Numerical Analysis of the Diffusive Transport Phenomena in Hypersonic Flows

A DISSERTATION
SUBMITTED TO THE FACULTY OF THE GRADUATE SCHOOL
OF THE UNIVERSITY OF MINNESOTA
BY

Chiara Amato

IN PARTIAL FULFILLMENT OF THE REQUIREMENTS
FOR THE DEGREE OF
DOCTOR OF PHILOSOPHY

Advisor: Graham V. Candler

July 2023

Saglie cu mme
e accumincia a cantà
insieme 'e nnote che ll'aria dà.
Senza guardà
tu continua a vulà,
mentre 'o viento
ce porta lla
addò ce stanno
'e pparole cchiù belle
e t' 'e piglie pe te 'mparà.

To Maria,
who taught me how to love, dream, and be brave.
We will never stop dancing.

Abstract

One of the main focuses of hypersonic research is understanding the relevant physicochemical phenomena that characterize hypersonic flows. Shock-induced heating and strong thermochemical non-equilibrium are significant occurrences in high-enthalpy, high-speed flows. To accurately simulate such flows, one must ensure that the relevant effects are described in the physical model of the gas. In conventional CFD, we solve a set of governing equations, the Navier-Stokes equations, that include the terms related to viscous dissipation, heat transfer, and mass diffusion of multiple chemical species present in the flow. These diffusive processes are a continuum manifestation of transport processes at the molecular scale. According to kinetic theory, the Boltzmann equation fully describes the statistical behavior of dilute gas mixtures. A mathematical link between the Boltzmann and the Navier-Stokes equations provides a complete description of the transport phenomena with additional terms neglected in the conventional continuum flow representation. Thus, with this work, we study the effects of diffusion transport properties and chemical kinetics by simulating different hypersonic flows in the near-continuum regime. In particular, we compare the solutions obtained with US3D, a code routinely used for complex hypersonic computational fluid dynamics simulations, and MGDS, a code capable of large-scale 3D Direct Simulation Monte Carlo calculations. This work is part of a long-term effort to strike a balance between computational efficiency and accuracy in simulations and perform eventually coupled hybrid CFD-DSMC simulations of hypersonic flows.

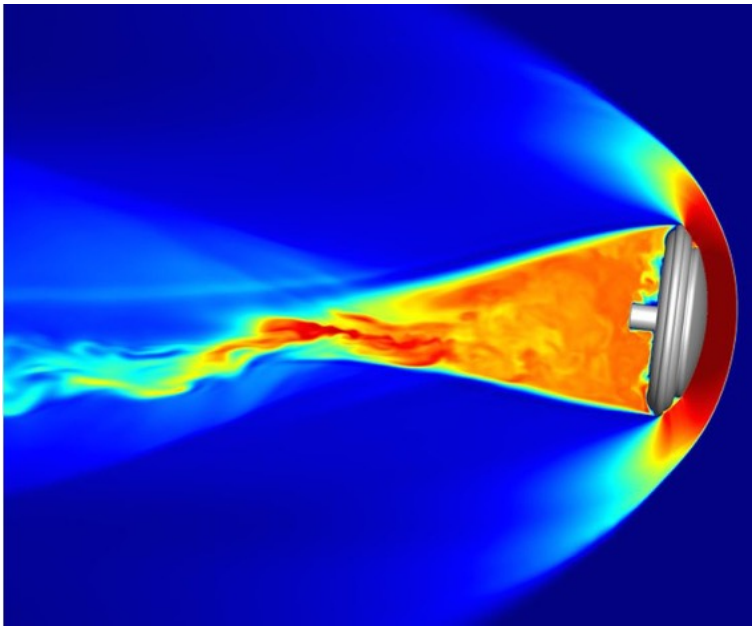

Figure 1: CFD simulation of the temperature distribution during the re-entry phase of a mission

Contents

Abstract **ii**

List of Figures **v**

List of Tables **vii**

Nomenclature **1**

1 Introduction **4**

1.1 Hypersonic Flows 5

1.2 Thesis Purpose and Motivation 7

1.3 Contents Overview 8

1.4 Literature Review 9

1.4.1 Relevant and Precedent Work 9

2 Physical Model for Hypersonic Flows **11**

2.1 Navier-Stokes Equations 11

2.1.1 Transport Fluxes 13

2.1.1.1 Diffusion Coefficient Models 13

2.1.1.2 Viscosity and Thermal Conductivity Models 15

2.1.2 Chemistry Models 17

2.1.2.1 Two-temperature Park Model 17

2.1.2.2 Modified Marrone-Treanor Model 18

2.1.2.3 Catalytic Wall Boundary Condition 19

2.2 The Boltzmann Equation and DSMC Method 20

2.3 Chapman-Enskog Theory 21

2.3.1 VHS Collision Integral Model 22

2.3.2 Mass Diffusion Flux 22

2.3.3 Viscous Stress Tensor 23

2.3.4 Heat Flux 23

2.4 Concluding Remarks 24

3 Test Cases **25**

3.1 One-dimensional Problems 25

3.2 Two-dimensional Problems 26

3.2.1 Shear Flow 27

3.2.2 Blunt Bodies 28

3.2.2.1 Cylinder 28

3.2.2.2 Sphere and Sphere Cone 31

3.3 Concluding Remarks 33

4 Results **34**

4.1 Monatomic gas test cases 34

4.2 Multi-Species Mixture 38

4.2.1 Cylinder 38

4.2.2 Sphere and Sphere cone 50

4.2.3 Sphere-cone 53

4.3 Concluding Remarks 55

5 Conclusions **57**

5.1 Contributions of this Work 57

5.2 Future work 59

Bibliography **62**

Appendix A Transport models parameters **65**

Appendix B Chapman-Enskog Parameters **66**

Appendix C Implementation in US3D **68**

C.1 Diffusion Transport Matrix Singularity due to Mass Conservation Constraint 68

C.2 Jacobian Formulation for the Full Diffusion Model Derived from CET 69

List of Figures

1 CFD simulation of the temperature distribution during the re-entry phase of a mission ii

3.1 A schematic diagram of the geometry for the one-dimensional problems 25
3.2 Sketch of CFD domain for the shear flow test case 27
3.3 Profiles for different grid sizes extracted at x=1 cm from the supersonic inlet. The cell number in the legend refers to the area of interest; the sponge layers are neglected. 28
3.4 Schematic of the CFD domain for the cylinder cases 29
3.5 Temperature profiles along the stagnation line for the cylinder case, obtained by using different mixtures and different grid sizes. 30
3.6 Sketch of transport phenomena in a boundary layer 30
3.7 Schematic of the CFD domain 32
3.8 Extraction locations for the sphere-cone case. 33

4.2 Extraction of the temperature profiles along the centerline in Fig. 3.1 for the one-dimensional flow problems. 35
4.3 Comparison of the solutions extracted at the stagnation line for the Argon flow around a cylinder, and obtained using DSMC and CFD with different diffusion viscosity models. 36
4.4 CFD solution of the two-dimensional shear flow problem 37
4.5 Gradient-length Knudsen num- ber distribution in the CFD flow field 38
4.6 Sketch of CFD domain for the shear flow test case 38
4.7 Mass fraction profiles comparison of MDGS and US3D solutions for the $4\,\mathrm{km\,s^{-1}}$ airflow around a cylinder case, extracted on the stagnation line and obtained with different chemical kinetics 40
4.8 Mass fraction profiles comparison of MDGS and US3D solutions for the $5\,\mathrm{km\,s^{-1}}$ airflow around a cylinder case, extracted on the stagnation line and obtained with different chemical kinetics 41

4.9 Mass fraction profiles comparison of MDGS and US3D solutions for the $6\,\mathrm{km\,s^{-1}}$ airflow around a cylinder case, extracted on the stagnation line and obtained with different chemical kinetics . . . 42
4.10 N2 mass fraction profiles comparison of the 6 km/s flow around a cylinder using different diffusion models on the stagnation line. . . . 43
4.11 Comparison of the diffusion contribution and mass fractions of N_2 for airflow around a cylinder at different free-stream velocities . . . 44
4.12 Mass fraction profiles comparison of MDGS and US3D solutions for the $4\,\mathrm{km\,s^{-1}}$ airflow around a cylinder case, extracted on the stagnation line and obtained with different diffusion models . . . 46
4.13 Mass fraction profiles comparison of MDGS and US3D solutions for the $5\,\mathrm{km\,s^{-1}}$ airflow around a cylinder case, extracted on the stagnation line and obtained with different diffusion models . . . 47
4.14 Mass fraction profiles comparison of MDGS and US3D solutions for the $6\,\mathrm{km\,s^{-1}}$ airflow around a cylinder case, extracted on the stagnation line and obtained with different diffusion models . . . 48
4.15 Comparison of the magnitude of diffusion terms due to the temperature and the pressure gradient to the full diffusion driving force for the cylinder at $4\,\mathrm{km\,s^{-1}}$. . . . 49
4.16 Comparison of the solutions obtained using the full diffusion model and considering only the Fickian contribution for the airflow around a sphere case. . . . 50
4.17 Magnitude comparison of the diffusion terms due to the temperature and the pressure gradient with the full diffusion driving force for the non-catalytic wall test case for the sphere case. . . . 51
4.18 Comparison of the solutions obtained using different catalytic efficiencies zoomed for the airflow around a sphere case in the near-wall region. . . . 52
4.19 Comparison of the wall heat flux obtained using different catalytic efficiencies γ for the airflow around a sphere case. . . . 53
4.20 Temperature contour plot for the sphere case with $\gamma = 0$ . . . 53
4.21 N_2 Mass fraction profiles at different locations for the sphere cone case. . . . 54
4.22 Magnitude comparison of diffusion terms due to the temperature and the pressure gradient with respect to the full diffusion driving force of N_2, O_2, N, and O for the non-catalytic wall test case. . . . 56

5.1 Comparison of the species mass fraction for the 8 km/s binary flow around a cylinder case on the stagnation line obtained using different diffusion models . . . 60
5.2 Zoom in the shock (on the top) and wall (on the bottom) areas for the 8 km/s binary flow around a cylinder case on the stagnation line obtained using different diffusion models . . . 61

List of Tables

3.1 Summary of the initial conditions for the Fourier and Couette test cases 26
3.2 Free stream conditions imposed for the shear flow test case. 27
3.3 Difference between the profiles obtained with the most refined grids 29
3.4 Initial and boundary conditions for the binary mixture test cases at a constant velocity and a constant density 31
3.5 Different inflow conditions for the air mixture test case imposed for the comparison study 31
3.6 Initial and boundary conditions for the sphere and sphere cone test cases 32

A.1 Blottner viscosity model coefficients. 65
A.2 VHS parameters 65

Nomenclature

ACRONYMS

BE	Boltzmann equation
CET	Chapman-Enskog theory
CFD	Computational Fluid Dynamics
CVD	Coupled Vibrational-Dissociation model
DPLR	Data-Parallel line relaxation
DSMC	Direct Simulation Monte-Carlo
MMT	Modified Marrone-Treanor model
MUSCL	Monotonic Upstream-centered Scheme for Conservation Laws
MUTATION++	MUlticomponent Thermodynamic And Transport properties for IONized gases
NSEs	Navier-Stokes Equations
SCEBD	Self-Consistent Effective Binary Diffusion
VHS	Variable Hard Sphere

GREEK LETTERS

κ	Thermal Conductivity
λ	Mean Free Path
μ	Mixture Viscosity
μ_∞	Free-Stream Viscosity
$\dot{\omega}_s$	Rate of Formation for Species s

ρ	Density
ρ_s	Partial density for species s
τ	Stress Tensor

LATIN LETTERS

$\mathbf{c}$	Particle velocity vector
$\mathcal{D}_{sp}$	Diffusion Coefficients of Species s into Species p
E	Energy
$\mathbf{F}^D$	transport flux tensor
f_v	Velocity distribution function
H	Enthalpy
I	Identity Matrix
$\mathbf{j}_s^D$	Mass Diffusion flux for Species s
Kn	Knudsen Number
Kn_{GL}	Gradient-length Knudsen Number
L	Characteristic Length scale of the Flow
MW_{gas}	Gas Molecular Weight
n	Number density
P	Pressure
$\mathbf{q}$	Heat Flux
$\mathbf{r}$	Position vector
R	Specific Gas Constant
R_∞	Universal Gas Constant
S	Total Number of Species
T	Temperature
t	Time

T_∞	Free-Stream Temperature
u, v	x and y Component of the Flow Velocity
$\mathbf{v}$	Velocity Vector
$\mathbf{v}_s^D$	Diffusivity Velocity for Species s
$\mathbf{v}_s$	Mean Velocity for Species s

SUPERSCRIPTS

D	Diffusion Component

SUBSCRIPTS

∞	Free-Stream Conditions
s	Species s

Chapter 1

Introduction

With a rich history and a profound impact on scientific, technological, and societal fronts, aerospace has been a cornerstone of human innovation and progress. This field encompasses the study, design, and exploration of the Earth's atmosphere and the vast expanse of outer space and has shaped our understanding of the universe and our place within it. Over the years, the field has been revolutionized by the advent of Computational Fluid Dynamics (CFD). This powerful tool has immensely impacted the understanding, analysis, and optimization of aerospace systems. With its ability to simulate and analyze fluid flow and its related phenomena, CFD has played a vital role in advancing the aerospace industry and humankind's achievements. From the mythical tales of humans flying to the invention of hot air balloons and dirigibles in the mid-18th century, pioneers and visionaries have strived to make manned flight possible. At the beginning of the 20th century, the Wright brothers had the breakthrough of powered flight. This unimaginable milestone ignited a rapid progression in aerospace technology, powered by dramatic historical reasons. Once warfare demands ceased, the development of propulsion technology led us to commercial aviation, military jets, and space exploration.

Nevertheless, as aerospace evolved, so did the challenges that engineers and designers faced. One of the crucial obstacles has been understanding and predicting the complex behavior of air and fluids around vehicles. Engineers relied heavily on wind tunnel testing and physical prototypes in order to study and advance aerodynamics. These methods were time-consuming, costly, and often limited in their capabilities. However, when computer technology advanced to a level that made complex simulations feasible during the late 1960s, powerful computational tools were developed to simulate and visualize the fluid flow. CFD emerged as a transformative tool for faster and more cost-effective design iterations. By numerically solving the governing equations of fluid dynamics, CFD accurately predicts the aerodynamic forces, pressures, and flow characteristics, thereby enabling engineers to optimize their designs for improved performance, fuel efficiency, and stability. One of the key advantages of CFD is its ability to simulate and investigate flow phenomena that are challenging to observe experimentally. For example, CFD has been instrumental in understanding the intricate

behavior of the flow during takeoff and landing, high-speed flight, and propulsion systems. By analyzing the flow patterns, engineers can identify areas of high drag, optimize wing shapes, and enhance vehicle performance. Moreover, CFD has played a crucial role in spacecraft design and exploration. It aids in analyzing re-entry and landing dynamics, the behavior of propellant flows, the aerodynamic stability and control of spacecraft during atmospheric entry, maneuvering in space, and the optimization of heat shield designs. Today, CFD has become an indispensable tool in aerospace engineering, used in the design of aircraft, rockets, and even space capsules.

1.1 Hypersonic Flows

Hypersonic flows are a class of flow characterized by a speed five times the speed of sound or higher. Vehicles that travel at these velocities are, for example, re-entry spacecraft, scramjets, ramjets, rockets, and others. At such high velocities, the gas and the surrounding environment undergo abrupt temperature, pressure, density, and velocity changes, generating complex multi-scale phenomena affecting the flow state. Thus, understanding the complexities involved in hypersonic flows is essential to design vehicles capable to endure prolonged exposure to this severe and sensitive environment. Thus, one of the main focuses of hypersonic research is to design computational tools that can accurately simulate the extreme conditions associated with such speeds, especially when replicating these conditions experimentally is as challenging and expensive as for these cases.

Simulating hypersonic flow presents the challenge of describing simultaneous phenomena happening at different length and time scales. At the macroscopic level, the high velocity of the vehicle compresses the air ahead of it, resulting in the formation of a bow shock. Within the shock front, the flow is subsonic, and its physical properties experience rapid and extreme changes over a minimal distance. In particular, the flow undergoes strong viscous dissipation generated by the intense shearing forces within the shock region and internal friction due to the rapid viscosity increase due to the shock compression. Furthermore, the high-temperature environment experienced by the flow favors heat transfer through mechanisms such as conduction, convection, and radiation.

These effects induce a significant increase in thermal energy, triggering phenomena at the microscopic level. The thermal energy can increase to the point of overcoming activation energy barriers allowing reactions such as dissociation, ionization, and the formation of new chemical species. these extreme flow conditions, non-equilibrium effects become prominent, resulting in a significant departure from thermodynamic equilibrium. There are many factors contributing to the rise of these thermochemical effects. At extremely high speeds and low densities, the speed of the molecules can be so high that the distance between collisions becomes significant, reducing the opportunities for molecular interactions. Consequently, the translational energy dominates, while the excitation of rotational and vibrational modes is limited by the less frequent collisions responsible for promoting these modes. Dissociation and ionization reactions produce reactive species that exacerbate the

energy imbalance and contribute to non-equilibrium behavior.

Understanding and adequately accounting for non-equilibrium effects are crucial for accurately modeling and predicting the behavior of hypersonic flows. Different numerical modeling techniques exist to approximate these multi-dimensional multi-physical problems approaching the solution from a different description of the flow. In CFD, we solve a closed set of governing equations describing the physical principles upon which all fluid dynamics is based, such as the conservation of mass, momentum, and energy. These equations are called the Navier-Stokes equations and are described in Chapter 2.1. It has been proven that the assumptions made for the NSE break down when translational non-equilibrium becomes strong.

The kinetic theory of gases, introduced in Chapter 2.2, defines a parameter called the Knudsen number Kn that helps us characterize the state of a gas flow and measure the non-equilibrium effects in a flow. This dimensionless number is the ratio between the mean free path λ and the characteristic length scale of the flow L.

$$Kn = \frac{\lambda}{L},$$

The mean free path λ is the average distance a molecule travels between successive collisions with other molecules and is defined in Equation 1.1.

$$\lambda = \frac{\mu_\infty}{\rho_\infty}\sqrt{\frac{\pi}{2R_\infty T_\infty}} \tag{1.1}$$

Here, μ_∞ is the free-stream viscosity, T_∞ is the free-stream temperature, $R = {}^{R_\infty}/_{MW_{gas}}$ is the specific gas constant.

Because of the complexity of hypersonic flows and the non-uniform distribution of their state, the Knudsen number varies within the flow field of hypersonic flows. They exhibit continuum-like and non-equilibrium behaviors. Thus, it is essential to identify the regions of the flow dominated by non-equilibrium effects to describe and model them in the numerical solver adequately. We can compute a modified version of the Knudsen number that scales with spatial variation of all the flow properties of interest and take the maximum to quantify the degree of local non-equilibrium. It is called the gradient-length Knudsen number [1] Kn_{GL} and is defined as:

$$Kn_{GL} = \max\left(\frac{\lambda}{Q}\left|\nabla Q\right|\right)_{Q\in[\rho,|\mathbf{V}|,T]}, \tag{1.2}$$

where Q can be the density, the bulk velocity defined as $|\mathbf{V}| = \sqrt{u^2+v^2}$, or the temperature.

It has been accepted in the community that CFD is an accurate model for flows characterized by $Kn_{GL} < 0.01$. Instead, particle-based methods, such as the Direct Simulation Monte Carlo (DSMC) method introduced in Chapter 2.2, must be used to accurately capture the motion and interactions

of individual particles to simulate higher Knudsen numbers. Since the macroscopic quantities of interest are eventually obtained from the steady-state solution by sampling the microscopic quantities over the time steps, it can be intuitive that DSMC can function as a reference point when compared to CFD solutions. By simulating molecular interactions, DSMC can accurately capture the behavior of non-equilibrium flows, offering a validating tool for the transport properties model in the CFD solver.

1.2 Thesis Purpose and Motivation

This dissertation provides a small contribution to a long-term effort to simulate and study the complexity of hypersonic flows using CFD methodology. A thorough understanding of hypersonic flows is necessary for developing tools capable of capturing a vast spectrum of physicochemical phenomena and accurately predicting the aerothermal loads on a hypersonic vehicle during its trajectory.

On one side, the state-of-the-art offers robust CFD codes capable of successfully simulating flows around hypersonic vehicles with the limitation that the assumptions made for the Navier-Stokes equations break down where the translational non-equilibrium is very strong. Under this condition, the compressible Navier-Stokes equations cannot fully capture the kinetic-scale effects that become important in the transitional regime between continuum and rarefied.

On the other side, DSMC can successfully simulate flow with non-equilibrium behaviors, but the simulation requirements become prohibitive in the continuum limit. The DSMC grid cells must be sized to the local mean free path to allow nearby particles to collide. Time steps must be smaller than the local mean collision time to move particles significantly toward the following collision. The complementary strengths of DSMC and CFD have pushed scientists to explore a hybrid methodology to solve flows in the transitional regime. However, coupling CFD and DSMC codes requires consistent physical models and creates the issue of combining very distinct methods.

This dissertation seeks to contribute to the preliminary analysis necessary to eventually couple the CFD and DSMC codes, which were developed in the Department of Aerospace Engineering and Mechanics at the University of Minnesota. The CFD simulations are performed using US3D, a solver for 3D complex hypersonic simulations, while the Molecular Gas Dynamic Simulator (MGDS) code is used for large-scale 3D DSMC calculations. The DSMC simulations and study were conducted by Michael Kroells at the University of Minnesota under Professor Schwartzentruber's guidance.

This thesis shows a detailed analysis of the diffusion transport properties' effect on hypersonic flows by comparing the CFD and DSMC solutions in the near-continuum regime. This flow regime, represented by $Kn = 0.001$, was selected because it is the best compromise between the validity of the NSE and the DSMC requirements. At this Knudsen number, the influence of kinetic-scale effects is minimal, and the DSMC simulation requirements are expensive but not prohibitive.

This work aims to analyze the accuracy of the available transport models and investigate how consistent modeling of the transport phenomena in the solvers affects the comparison. In particular, we will initially compare the DSMC results with the solutions obtained with conventional CFD. Here, mixing rules and diffusion laws close the governing equations where the transport fluxes depend on the steep gradients of the local flow field variables, such as species concentrations, velocity, and temperature. Whereas, according to the kinetic theory, the Boltzmann equation fully describes the statistical behavior of gas mixtures. Thus, DSMC naturally captures the macroscopic transport properties as a function of the collision dynamics and the cross-section models used.

If we want to make the CFD and the DSMC code, we must describe the transport fluxes using the Chapman-Enskog approximation theory with the VHS-based collision integrals. In the early twentieth century, Chapman and Enskog independently provided the mathematical relation between the Boltzmann and the Navier-Stokes equations showing a complete description of the transport phenomena. Even though they derived transport coefficients such as viscosity and thermal conductivity, Chapman and Enskog included other transport terms that contribute to mass and energy diffusion in the molecular conservation equations. These additional terms represent how heat and mass transfer are related in non-equilibrium conditions due to simultaneous physicochemical events. Specifically, two terms appear in the mass conservation equation: thermal diffusion, also known as the Soret term, and a pressure term that accounts for the mass diffusion due to a temperature and a pressure gradient, respectively. The Dufour term is an additional term in the energy conservation equation and represents the contribution of species concentration gradient to the energy transfer. Historically, these extra terms are assumed to be negligible in hypersonic flows and are usually omitted from CFD simulations.

This study analyzes the importance of solving the full diffusion model derived from the Chapman-Enskog theory, identifies the dominating phenomena, and assesses their contributions to the hypersonic flow fields in the near-continuum regime. This insight would lead to the development of a more accurate description of the transport properties for Computational Fluid Dynamics applications in non-equilibrium conditions. In the following paragraph, we offer an overview and a short description of each chapter, followed by the central literature that supports this work.

1.3 Contents Overview

The following five chapters capture the work done for this dissertation and are organized in the following manner.

Chapter 1 contextualizes this research in the state-of-the-art, describes hypersonic flows and their characteristics in detail. It explains the main assumptions and states the goals and purpose of this thesis. **Chapter 2** presents the set of equations we solve numerically with the CFD solver and the different transport and chemical models utilized for this study. It introduces the basics

of kinetic theory and the DSMC method used as a reference for the CFD analysis. **Chapter 3** describes the problems we are solving in Chapter 4. It is divided into two parts in which, for each problem, we describe the geometries, the grid, and the initial and the boundary conditions. The first part is dedicated to one-dimensional problems, the Fourier and Couette flow. The second part gathers all the information relevant to the two-dimensional test cases. This analysis studies a shear flow and the flows around blunt bodies. **Chapter 4** demonstrates all the results used in this dissertation to analyze the transport phenomena. As in the previous one, this chapter is split into two main sections. The first part is dedicated to the validation study conducted with a monoatomic gas. The second part analyzes the results of multi-species mixtures to analyze the diffusive phenomena between species. **Chapter 5** concludes the dissertation by summarizing the main conclusions drawn by analysis of the results.

1.4 Literature Review

This paragraph offers a panoramic view of the work on which this dissertation stands. We introduce the papers that preceded this dissertation and give a foundation for our choice.

1.4.1 Relevant and Precedent Work

Hybrid particle-continuum simulations of nonequilibrium hypersonic blunt-body flow fields.

Schwartzentruber, T.E., Scalabrin, L.C. and Boyd, I.D., Journal of Thermophysics and Heat Transfer, 22(1), pp.29-37.

Schwartzentruber et al. studied simple hypersonic flows of N_2 around blunt bodies using different numerical method to analyze non-equilibrium behaviors in these flows. In particular, they simulated those flows using DSMC, NSE and a modular particle-continuum numerical method that solves the NSE in near-equilibrium regions and uses DSMC in non-equilibrium regions. Through the analysis of the velocity distributions for two-dimensional flows at different Mach numbers, Schwartzentruber et al. showed that regions such as the inside of the shock wake and the near-wake region deviate significantly from the near-equilibrium distribution. They were the first to successfully replicate DSMC solutions using a hybrid particle–continuum numerical method. Also, they showed the accuracy of the NSE in regions with gradient-length Knudsen numbers smaller than $Kn_{GL} = 0.05$. Finally, they proved that the Kn_{GL} is a good tool to predict the difference between the NS and the DSMC solutions.

Transport properties of partially ionized and unmagnetized plasmas.

Magin, T.E. and Degrez, G., 2004. Physical Review E, 70(4), p.046412.

Magin et al. presented a complete study of transport phenomena in partially ionized and unmagnetized plasmas. They derived the model from the kinetic theory and implemented new constrained integral equations from a modified Chapman-Enskog perturbative method to treat thermal non-equilibrium. Furthermore, the authors commented on the comparative study of the results obtained with their new kinetic treatment of the transport fluxes to literature data when solving for two-temperature plasmas. In conclusion, the theoretical study shown in the paper introduces a practical formulation of a transport algorithm for fluid dynamics applications.

Transport algorithms for partially ionized and unmagnetized plasmas

Magin, T.E. and Degrez, G., 2004. Journal of Computational Physics, 198(2), pp.424-449

In this paper, Magin et al. analyzed the new transport properties formulation, introduced in the previous paper, from a computational point of view. The transport algorithm overcomes the singularity of the diffusion matrix mass with a symmetric and non-singular Stefan–Maxwell matrix, including the mass constraint, in the case of direct methods. The authors studied the accuracy and efficiency of the algorithm using an 11-species air plasma in local thermo-equilibrium at atmospheric pressure. In particular, they extracted and compared the transport coefficients, fluxes, and their relative error using different models. The transport algorithm can be extended to simulate thermo-chemical non-equilibrium conditions.

Multicomponent flow modeling

Giovangigli, V., 2012. Science China Mathematics, 55, pp.285-308.

Giovangigli presented a multicomponent flow model derived from the kinetic theory of gases. They described numerical algorithms used to solve complex chemistry flows, focusing on studying multicomponent transport properties and their impact on the flow field. Giovangigli's model can be used to solve gas mixtures in fully vibrational non-equilibrium. The transport model and algorithm studied by Magin et al. and introduced in the previous two papers were inspired by this work.

Soret and Dufour effects on magnetohydrodynamic (MHD) flow of Casson fluid.

Hayat, T., Shehzad, S.A. and Alsaedi, A., 2012. Applied Mathematics and Mechanics, 33, pp.1301-1312.

The Soret and Dufour terms are investigated in the study of non-Newtonian fluid flows generated by a stretching sheet during the extrusion of polymers. In particular, the paper studies the boundary layer flow in the regime of two-dimensional flows of the Casson fluid. They showed how the Soret and the Dufour terms affect the concentration and temperature profiles and the boundary layer thickness.

Chapter 2

Physical Model for Hypersonic Flows

This chapter is dedicated to the mathematical description of hypersonic flows. Having explained in the introduction, these flows present a broad spectrum of physical and chemical phenomena at the different scales of length and time. Thus, an accurate model of hypersonic flows must fully represent the macroscopic phenomena, such as the strong viscous dissipation and heat transfer caused by sharp velocity, temperature, and pressure gradients. Moreover, since these flows are characterized by translational thermodynamic non-equilibrium, especially in the shock and near-wall regions due to the flow's high enthalpy, their numerical model must also incorporate the description of the molecular interactions between the particles and the wall. Recent research has provided numerical techniques to simulate hypersonic flows using either a continuum approach or particle methods in order to solve these complicated problems. This chapter provides a detailed description of the chosen numerical methods by concentrating on the CFD models. Thus, Chapter 2 starts by explaining the conservation equations of mass, momentum and energy for reacting flows, and the description of the component, including thermodynamic, transport, and chemical terms. Subsequently, the chapter describes the kinetic theory fundamentals and particle methods to explain the reasons behind comparing solutions obtained using these methods. Finally, Chapter 2 concludes with an analysis of the Chapman-Enskog theory that provides a mathematical link between the continuum and kinetic description of the flow mathematically. This dissertation implements the transport properties model based on CET to show the improvement in the accuracy of CFD simulations in the regions of strong translational non-equilibrium where the assumptions made for the Navier-Stokes equations start to break down.

2.1 Navier-Stokes Equations

From a macroscopic perspective, the compressible Navier-Stokes equations mathematically represent the conservation of mass, momentum, and energy for flows in hypersonic conditions. The NSEs are a coupled system of non-linear partial differential equations that describe the fundamental

physical principles upon which all fluid dynamics is based, such as the conservation of mass and energy and Newton's second law.

The NSEs are summarized in Equations 2.1, 2.2, and 2.3 in their conservative forms. They are the species continuity equations for the species s composing the mixture, the momentum continuity, and the total energy continuity equations, respectively.

$$\frac{\partial \rho_s}{\partial t} + \nabla (\rho_s \mathbf{v}) + \nabla \mathbf{j}_s^D = \dot{\omega}_s \quad \forall s \in S \tag{2.1}$$

$$\frac{\partial \rho \mathbf{v}}{\partial t} + \nabla [\rho(\mathbf{v} \times \mathbf{v}) + PI] - \nabla \underline{\tau} = 0 \tag{2.2}$$

$$\frac{\partial \rho E}{\partial t} + \nabla (\rho \mathbf{v} H) - \nabla (\underline{\tau} \mathbf{v} - \mathbf{q}) = 0 \tag{2.3}$$

In Eqs. 2.1, ρ_s is the partial density for species s, $\mathbf{v}$ is the mass-averages mixture velocity, $\dot{\omega}_s$ is the rate of species formation, and S is the total number of species. The species continuity equations, expressed by Eq. 2.4, are linearly dependent due to the constraint of the mass conservation principle.

$$\sum_{s=1}^{S} \mathbf{j}_s^D = \sum_{s=1}^{S} \rho_s \mathbf{v}_s^D = 0 \tag{2.4}$$

where $\mathbf{v}_s^D$ is the diffusivity velocity for species s. We obtain the total mass continuity equation by summing all Equations 2.1 over the total number of species S.

$$\frac{\partial \rho}{\partial t} + \nabla (\rho \mathbf{v}) = 0$$

The mass-averaged mixture velocity, $\mathbf{v}$, and the diffusivity velocity for species s, $\mathbf{v}_s^D$, are defined and related by Eqs. 2.1 and 2.4, where $\mathbf{v}_s$ is the mean velocity for species s.

$$\mathbf{v} = \sum_{s=1}^{S} \frac{\rho_s}{\rho} \mathbf{v}_s \qquad \mathbf{v}_s^D = \mathbf{v} - \mathbf{v}_s \tag{2.5}$$

In Eq. 2.2 and 2.3, P is the flow pressure, I is an identity matrix, E is the total energy defined as the sum of the internal and the kinetic energy $E = e + \frac{\mathbf{v}^2}{2}$, and H is the total enthalpy described by $H = E + \frac{p}{\rho}$. The last term on the left-hand side in each governing equation composes the transport flux tensor $\mathbf{F}^D$, as shown by Eq. 2.6:

$$\nabla \mathbf{F}^D = \nabla \begin{bmatrix} -\mathbf{j}_s^D & \underline{\tau} & \underline{\tau}\mathbf{v} - \mathbf{q} \end{bmatrix}^T . \tag{2.6}$$

where $\mathbf{j}_s^D$, τ, and $\mathbf{q}$ are the mass flux of the species s due to diffusion, the viscous stress tensor, and the heat flux, respectively. These quantities are known as transport fluxes, and describe the

exchange of mass, momentum, and energy when the gradients of species concentration, velocity, and temperature are present. In conventional CFD, several models provide a mathematical description of the transport fluxes. These quantities are the central focus of this dissertation which investigates the available models in the literature and studies the implementation of the molecular description of transport properties derived from CET. By comparing these different models, we analyze and show how essential it is to accurately describe the transport properties when simulating hypersonic flows in the near continuum regime.

2.1.1 Transport Fluxes

The transport fluxes in the NSEs are a macroscopic representation of the processes occurring at the molecular scale in high-enthalpy flows due to the thermochemical non-equilibrium. In the continuum description of a non-equilibrium gas, the transport processes are described by constitutive relations where fluxes are directly proportional to the state variables' gradients and a coefficient for each transport phenomenon. These coefficients, called transport properties, contain the different molecular properties being carried around by the particles randomly moving in non-equilibrium conditions. Different models can offer the closing equations necessary to solve transport properties and fluxes for CFD solvers. In the current state-of-the-art of hypersonic research, the transport fluxes in the mass, momentum, and energy equations are described using Fick's, Newton's, and Fourier's laws, summarized here for completeness.

$$
\begin{aligned}
&\mathbf{j}_s^D = \rho_s \mathbf{v}_s^D = -\rho \mathcal{D}_{sp} \nabla \left(\frac{\rho_s}{\rho} \right) \quad \text{with} \;\; s,\, p \in \mathcal{S} && \text{Fick's law of diffusion} \\
&\underline{\tau} = \mu \left[\nabla \mathbf{v} + (\nabla \mathbf{v})^T - \frac{2}{3} (\nabla \cdot \mathbf{v}) \mathbf{I} \right] && \text{General Newton's law of viscosity} \\
&\mathbf{q} = -\kappa \nabla T - \sum_{s \in S} h_s \mathbf{j}_s && \text{Fourier's law of heat conduction and enthalpy diffusion}
\end{aligned}
\tag{2.7}
$$

The mixture transport properties in Eq. 2.7 are $\mathcal{D}_{sp}$, the diffusion coefficients of species s into species p, while μ and κ are the mixture viscosity and thermal conductivity, respectively. They represent the macroscopic description of the molecular transport processes caused by translational thermochemical non-equilibrium. In conventional CFD, the transport properties can be obtained from experimental data or can be estimated by using the equations of state or empirical correlations. In this study, several models have been compared and are described in the following paragraph.

2.1.1.1 Diffusion Coefficient Models

Understanding the mechanics of diffusion is fundamental to accurately predict the complex behavior of multi-component flows, particularly in the environment with extreme conditions such as high-

speed and high-temperature hypersonic flows. Accurate diffusion modeling is vital for capturing the species concentrations and distributions, which, in turn, affect heat transfer rates, chemical reactions, and overall flow characteristics. This section presents the available diffusion models in CFD simulations, specifically by emphasizing the models for multi-component flows. These models range from simple to more complex formulations, depending on the problem's nature and the desired accuracy level. However, these approximations may not capture all species' detailed interactions and diffusion behavior in complex mixtures. In some cases, more sophisticated models, such as the multi-component diffusion models based on the kinetic theory, are required to simulate diffusion in multi-component gas mixtures accurately.

Diffusion Coefficient Derived from Constant Schmidt Number

The simplest model available in the literature is the Constant Schmidt Number diffusion model, which assumes the diffusivity remains constant throughout the flow domain and can be related to the molecular diffusivity using the Schmidt number, Sc. It is a non-dimensional quantity defined as the ratio of the viscous diffusion rate and the mass diffusion rate:

$$Sc = \frac{\mu}{\rho \mathcal{D}} = \frac{\text{viscous diffusion rate}}{\text{molecular diffusion rate}}. \tag{2.8}$$

When using this model, the diffusion coefficient $\mathcal{D}$, derived from the Eq. 2.8, is uniform and independent of the local flow conditions. While this dimensionless number couples the momentum and mass diffusion convection processes, it does not represent the molecular interaction between the species in the presence of a mixture since it is treated as a monatomic gas.

Self-Consistent Effective Binary Diffusion Approximation

The Self-Consistent Effective Binary Diffusion (SCEBD) [2, 3] model supplies an effective diffusion coefficient that considers the interactions between different species and captures the averaged diffusion behavior of the mixture without solving the full linear system of equations derived from the kinetic theory. This model, described by Ramshaw et al. [2, 3], provides a simplified representation of multi-component diffusion by defining an effective binary mixture in which the two components are each species s and a pseudo compound that represents all the remaining species. In particular, Ramshaw et al. [2, 3] define the effective binary diffusivities D_s, as follows:

$$D_s \equiv \left(1 - \frac{w_s}{w}\right) \left(\sum_{p \in S}^{p \neq s} \frac{X_p}{\mathcal{D}_{sp}}\right)^{-1} \qquad \forall s \in S,$$

where w_s and w are the weighting coefficients chosen to accurately represent the different species forming the pseudo species, X_p is the molar fraction of species p, and $\mathcal{D}_{sp}$ is the actual binary

diffusion coefficient between the species s and p and is a function of the chosen collision cross-sections[1]. Ramshaw et al. [2, 3] took advantage of the exact solution for a binary mixture of the linear system based on the kinetic theory and rearranged the equations obtaining a formulation for the self-consistent diffusion fluxes $\mathbf{j}_s^D$ which is given by

$$\mathbf{j}_s^D = -cM_sD_s\mathbf{d}_s^D + Y_sc\sum_p M_pD_p\mathbf{d}_p^D, \tag{2.9}$$

where M_s is the molecular weight of species s, $c = \sum_s \rho_s M_s$ is the total molar concentration, and Y_s is the mass fraction for species s. The details of the model, the definition of the weighting coefficients, and the reasoning behind this approximation can be found in the reference [2, 3].

2.1.1.2 Viscosity and Thermal Conductivity Models

As for the diffusion coefficient, several types of approximation can provide an expression for the mixture viscosity μ and thermal conductivity κ. conventional CFD models evaluate them using mixing rules, temperature-dependent laws, and curve fitting based on collision cross-section data. The following section summarizes the models used in this study in order to provide a complete overview of the tools utilized in this dissertation.

Blottner Viscosity Fits with Wilke Mixing Rule

Wilke's mixing rule [5] is a semi-empirical equation that expresses the mixture viscosity μ and thermal conductivity κ as a function of the mixture individual components properties, as shown in Eq. 2.10.

$$\mu = \sum_{s\in S}\frac{X_s\mu_s}{\phi_s} \qquad \text{and} \qquad \kappa = \sum_{s\in S}\frac{X_s\kappa_s}{\phi_s}, \tag{2.10}$$

where

$$\phi_s = \sum_{p\in S} X_p\left[1+\sqrt{\frac{\mu_s}{\mu_p}}\left(\frac{M_p}{M_s}\right)^{\frac{1}{4}}\right]^2\left[\sqrt{8\left(1+\frac{M_s}{M_p}\right)}\right],$$

μ_s and κ_s are the species' viscosity and thermal conductivity. They are defined respectively by Blottner curve fits [6] and Eucken relation, which are displayed in the following equations:

$$\mu_s = 0.1\exp\left[(A_s\ln T + B_s)\ln T + C_s\right], \tag{2.11}$$

$$\kappa_s = \frac{5}{2}\mu_s c_{vs}, \tag{2.12}$$

[1]The current study uses the SCEBD approximation in conjunction with the Gupta-Yos collision integral-based transport properties model [4], explained in Section 2.1.1.2.

where A_s, B_s, and C_s are tabulated and can be found in the Appendix B. The Blottner curve fits are valid for temperatures up to 10,000 K.

Sutherland's Law for Viscosity

Sutherland's viscosity law [7] is an empirical relationship that defines the mixture viscosity and thermal conductivity as follows:

$$\mu = \mu_{ref} \left(\frac{T}{T_{ref}} \right)^{\frac{3}{2}} \frac{T_{ref} + S_\mu}{T + S_\mu},$$
$$\kappa = \kappa_{ref} \left(\frac{T}{T_{ref}} \right)^{\frac{3}{2}} \frac{T_{ref} + S_\kappa}{T + S_\kappa},$$

where S_μ and S_κ are the Sutherland constants representing the temperature sensitivity of the gas's dynamic viscosity, T_{ref} is the reference temperature usually set at $T_{ref} = 250\,\mathrm{K}$, and μ_{ref} and κ_{ref} are the viscosity and the thermal conductivity at T_{ref}.

Sutherland law is widely used for modeling the viscosity of gases at high temperatures, where the effects of molecular interactions become significant. It is important to note that Sutherland law assumes that the gas is in a state of local thermodynamic equilibrium. Thus, it may not accurately represent the behavior of gases with complex molecular interactions.

Gupta-Yos Collision Integral-based Transport Properties

Gupta et al. [4] provide a formulation for transport properties based on the multi-component diffusion using the assumptions of equilibrium reacting gas mixture. According to Gupta et al. [4] all the species in the mixture move with the same velocity or are in the stationary stage. In particular, they complete the mixture viscosity and thermal conductivity as follows:

$$\mu = \frac{1}{N_A} \sum_{s \in S} \frac{M_s X_s}{\sum_{p \in S} X_p \Delta_{sp}^{(2)}},$$
$$\kappa = \frac{15}{4} k \sum_{s \in S} \frac{X_s}{\sum_{p \in S} \alpha_{sp} X_p \Delta_{sp}^{(2)}} + \frac{1}{N_A} \sum_{s \in S}, \frac{c_{p_s}^{(int)} M_s X_s}{\sum_{p \in S} X_p \Delta_{sp}^{(1)}}$$
$$\alpha_{sp} = 1 + \left(1 - \frac{M_s}{M_p}\right) \left(0.45 - 2.54 \frac{M_s}{M_p}\right) \left(1 + \frac{M_s}{M_p}\right)^{-2},$$

where $\Delta_{sp}^{(1)}$ and $\Delta_{sp}^{(2)}$ are coefficients proportional to the collision integrals $\pi \bar{\Omega}_{sp}^{(l,l)}$, and are defined in Eqs. 2.13 and 2.14:

$$\Delta_{sp}^{(1)} = \frac{8}{3} \left(\frac{2 M_s M_p}{\pi R T \left(M_s + M_p\right)} \right)^{12} \pi \bar{\Omega}_{sp}^{(1,1)}, \tag{2.13}$$

$$\Delta_{sp}^{(2)} = \frac{16}{5}\left(\frac{2M_sM_p}{\pi RT\left(M_s+M_p\right)}\right)^{12}\pi\bar{\Omega}_{sp}^{(2,2)}. \tag{2.14}$$

The collision integrals $\pi\bar{\Omega}_{sp}^{(l,l)}$ represent the average collision cross-section between the species s and p and are defined through temperature-dependent curve fits at constant pressure:

$$\pi\bar{\Omega}_{sp}^{(1,1)} = \exp(D_1)T^{(A_1\ln T^2+B_1\ln T+C_1)},$$
$$\pi\bar{\Omega}_{sp}^{(2,2)} = \exp(D_2)T^{(A_2\ln T^2+B_2\ln T+C_2)},$$

where A_1-D_1 and A_2-D_2 are tabulated for each species.

2.1.2 Chemistry Models

When simulating a multi-component gas mixture, the physical model must describe the chemical reactions between each species and their properties. As shown in Chapter 3, the only reacting mixture considered in this study is a five-species airflow, which is made of N_2, O_s, NO, N, and O. The relevant reactions modeled in the computation tools are:

$$\left.\begin{array}{lcl} N_2+M & \Leftrightarrow & N+N+M \\ O_2+M & \Leftrightarrow & O+O+M \\ NO+M & \Leftrightarrow & N+O+M \end{array}\right\}\text{Dissociation reactions} \tag{2.15}$$

$$\left.\begin{array}{lcl} N_2+O & \Leftrightarrow & NO+N \\ NO+O & \Leftrightarrow & O_2+N \end{array}\right\}\text{Exchange reactions} \tag{2.16}$$

The forward reactions in Equation 2.15 are the dissociation of the diatomic species N_2, O_2, and NO with any species M acting as an inert collision partner, which provides the necessary kinetic energy to break the chemical bond during the reaction. Conversely, the backward reactions are the recombination of the N and O atoms in the possible diatomic products, while the arbitrary species M absorbs the released energy. The reactions in Equation 2.16 are the Zeldovich exchange reactions representing oxidation of nitrogen and NOx formation. The following paragraphs describe the two models used in the current analysis to describe chemical reaction rates for the chosen reactions.

Furthermore, the vibrational energy is approximated as a simple harmonic oscillator, while the electronic energy is neglected for this analysis. This model and approximation are chosen so that the CFD solver is consistent with the DSMC internal energy model.

2.1.2.1 Two-temperature Park Model

The two-temperature Park model is one of the most studied models in the literature for hypersonic applications. The dissociation rates are assumed to be governed by an effective temperature which

is given by the geometric mean of the vibrational and translational-rotational temperatures, $T_{Ef} = \sqrt{TT_v}$. This effective temperature approximates the reduction of the dissociation rate due to vibrational non-equilibrium behind a shock wave. Thus, the forward and the backward reaction rate coefficients are expressed in a modified Arrhenius form for the generic reaction r:

$$k_{f_r}(T_{Ef}) = C_{fr_r} T_{Ef}^{\eta_r} \exp(\frac{\theta_r}{T_{Ef}})$$
$$k_{b_r}(T_{Ef}) = \frac{k_{f_r}(T_{Ef})}{K_{c_r}}$$

C_{fr_r}, η_r, θ_r, and K_{c_r} are tabulated constants for each r reaction.

2.1.2.2 Modified Marrone-Treanor Model

The Modified Marrone-Treanor model [8–10] represents the dissociation rates due to vibrational non-equilibrium behind a shock wave with a temperature-dependent complex function based on the QCT analysis of the high-fidelity potential energy surfaces for the air dissociation reactions. This method developed by Chaudhry et al. [8, 9] integrates the effect of the rotational energy to the classical Marrone-Treanor preferential dissociation model. This method is a coupled vibrational-dissociation (CVD) model that includes dissociation as a contributing factor in the thermal non-equilibrium with the assumption that vibrationally-excited molecules are more likely to dissociate. Chaudhry et al. [8, 9] implemented the method by using ab-initio quantum chemistry data (QCT) based on potential energy surfaces developed by the Truhlar group at the University of Minnesota [11–13]. The following relation describes the forward reaction rates:

$$k_{f_r}(T_{tr}, T_v) = k_{arr}(T_{tr}) Z(T_{tr}, T_v)$$

where:

- $k_{arr}(T_{tr})$ is the modified Arrhenius reaction rates:

  $$k_{arr_m}(T_{tr}) = C T_{tr}^n \exp\left(-\frac{T_D}{\cdot} T_{tr}\right)$$

  T_D is the characteristic temperature of dissociation, and C and n are tabulated coefficients defined for all the collision pairs [10].

- $Z(T_{tr}, T_v)$ is a non-equilibrium correction factor, defined as

  $$Z(T_{tr}, T_v) = \frac{Q(T_{tr})Q(T_F)}{Q(T_v)Q(T_{-U})} \qquad \text{with} \qquad Q(T) = \frac{1 - \exp(-T_D/T)}{1 - \exp(-\theta_v/T)},$$

  where:

- T_F and T_{-U} pseudotemperatures [10];
- $Q(T_x)$ are the approximate vibrational partition functions;
- θ_v is the characteristic vibrational temperature.

Furthermore, the vibrational energy change per dissociation is described as follows:

$$-\frac{\langle \varepsilon_{vib} \rangle_d}{k_B} = \frac{\theta_V}{\exp\left(\theta_V / T_F\right)} - \frac{T_D}{\exp\left(T_D / T_{tr}\right)}.$$

The QCT data are collected for the reactions of $N_2 + N_2$, $N_2 + N$, $N_2 + O_2$, $O_2 + O$, and $O_2 + O$ obtained by using Boltzmann distributions at translational and vibrational temperatures T_{tr} and T_v. The database is built without electronic energy and assumes all reactants are at the ground electronic state. However, the dissociation rate of the oxygen is multiplied by a correction factor $\eta = 16/3$ for all temperatures. This correction was initially proposed by Nikitin [14] to represent that O2 is characterized by two low-lying electronic energy levels.

2.1.2.3 Catalytic Wall Boundary Condition

A hypersonic ablative TPS made of catalytic material can significantly influence the chemical reactions occurring at the boundary layer and the overall flow characteristics. Since the extra transport property and flux terms are a function of the species concentration and the temperature gradients, we investigate the effects of catalysis when the full diffusion model is considered. A catalytic wall boundary condition incorporates a surface reaction rate term that represents the enhanced chemical reactions due to the presence of a catalytic surface. This term accounts for the increased recombination and energy exchange between the gas molecules and the surface. In particular, two-body recombination reactions are considered for this study for atomic Nitrogen and Oxygen.

A dimensionless parameter γ, called catalytic efficiency, is defined to quantify the portion of atoms that recombines after impinging the wall. It is equal to the ratio between the flux of atoms that recombine on the surface and the total mass flux that impinge on the surface, as shown in the following equation:

$$\gamma = \frac{\dot{m}_{rec}}{\dot{m}_{imp}}.$$

This boundary condition is implemented by balancing the mass flux of the relevant species at the wall:

$$\rho_s \mathbf{v}_s^D = \omega_s = \rho_s \mathbf{v}_s^{\dot{m}} = \rho_s \gamma \sqrt{\frac{k_B T_w}{2\pi m_s}},$$

where $\mathbf{v}_s^{\dot{m}}$ is the catalytic recombination speed and is a function of the thermal speed of species s.

2.2 The Boltzmann Equation and DSMC Method

The kinetic theory is a fundamental framework used to explain the dynamics of gases in a state of non-equilibrium, providing insights into their macroscopic properties based on the interactions and motions of individual particles at the microscopic level. The equation that describes such gases is one of the fundamental equations of statistical physics: the single-particle distribution Boltzmann transport equation, shown by Equation 2.17.

$$\frac{\partial}{\partial t}\left(nf_v\right) + \mathbf{c}\frac{\partial}{\partial \mathbf{r}}\left(nf_v\right) = \Delta\left[f_v\right]_{coll} \tag{2.17}$$

Eq. 2.17 is a non-linear integrodifferential equation describing the time evolution of the velocity distribution function f_v in terms of particles' motion $\mathbf{c}\frac{\partial}{\partial \mathbf{r}}\left(nf_v\right)$ and particles' collision $\Delta\left[f_v\right]_{coll}$. In Eq. 2.17, n is the number density, $\mathbf{r} = (x, y, z)$ is the position vector, and $\mathbf{c} = (v_x, v_y, v_z)$ the particle velocity vector. The velocity distribution function f_v is a one-particle distribution function defining the probability of finding a fixed particle in a specific point in the phase-space $(\mathbf{r}, \mathbf{c})$, at time t. Furthermore, the collision term $\Delta\left[f_v\right]_{coll}$, the right-hand side of Eq. 2.17, is a function of the relative speed between colliding particles and the chosen collision cross-section model. The assumptions underlying this theory are that the particles are in constant random motion following a straight trajectory, and they are considered point masses because their size is negligible with respect to the mean free path[2]. Moreover, the collisions are assumed to be perfectly elastic. Thus, no energy is lost, and the system's total energy, including both kinetic and potential energy, is conserved in collisions.

The most popular numerical method used to approximate the BE is the Direct Simulation Monte Carlo (DSMC) particle method developed by Bird [15]. This method [16, 17] statistically simulates the Boltzmann equation in the limit of an infinite number of particles. In particular, a large number of particles are simulated to randomly move in a discretized six-dimensional phase-space for a specific time step Δt and randomly collide with other particles or the solid surface. Thus, instead of tracking individual gas particles, the method divides the simulation domain into computational cells and proceeds using discrete time steps. The gas particles are grouped in each cell and represented as statistical "simulation particles." The grid size must be sized to the local mean free path[2] to allow nearby particles to collide, and the time steps must be smaller than the local mean collision time[2] to move particles significantly toward the following collision. The DSMC method has been successfully used to accurately model rarefied gas flows characterized by a Knudsen number greater than 1. Even if the DSMC method can be extended to model continuum flows, the application of DSMC can become computationally too expensive and sometimes inaccessible because of the grid and time step requirements scaling with the mean free path and mean collision time, respectively.

[2]Defined in Chapter 1

However, since the macroscopic quantities of interest are eventually obtained from the steady-state solution by sampling the microscopic quantities over the time steps, it is intuitive that DSMC can function as a reference point when compared to CFD solutions. By simulating molecular interactions, DSMC can accurately capture the behavior of non-equilibrium flows, offering a validating tool for the transport properties model in the CFD solver. In particular, this study aims to use DSMC as reference data to assess the accuracy of the CFD simulations, validate the numerical models, and identify areas of improvement for flows in the near continuum regime.

2.3 Chapman-Enskog Theory

In 1916 and 1917, Sidney Chapman in Cambridge and David Enskog in Sweden independently provided the mathematical relation between the Boltzmann and the Navier-Stokes equations showing a complete description of the transport phenomena [18]. First, they derived the Maxwell Equation of change by taking the zeroth, first, and second moments of the BE, obtaining an equation independent from the velocity space and function of averaged values:

$$\frac{\partial}{\partial t}\left(n\overline{Q}\right) + \frac{\partial}{\partial \mathbf{r}}\left(n\overline{\mathbf{c}Q}\right) = \Delta\left[Q\right]_{coll}, \tag{2.18}$$

where $\overline{Q}$ is an arbitrary particle property, and $\Delta\left[Q\right]_{coll}$ represent the rate of change of the particle property Q due to intermolecular collision.

Thus, they determined that a first-order perturbed Maxwell velocity distribution function is the precise function that reduces the Boltzmann equation to the Navier–Stokes equations. As shown in the following paragraphs, the generalized Chapman-Enskog solution of the BE matches the conservation equations of mass, momentum, and energy, including the transport terms in the Fickian, Newtonian, and Fourier forms and an expression in terms of molecular parameters for the diffusivity coefficients, viscosity, and thermal conductivity. In addition, CET presents an extra transport property for each species s and additional transport terms in the mass and energy equations. These terms are functions of the concentration, pressure, and temperature gradients and link the multi-species diffusion and energy transport. These new transport properties and terms are usually neglected in conventional CFD modeling.

The goal of this study is to identify and quantify all the transport and diffusion phenomena typical of hypersonic flows by implementing the transport model derived from CET and studying the relevance by making meaningful comparisons in the limit of near-equilibrium between numerical solutions obtained with a CFD and a DSMC solver. The following paragraphs show the set of linear systems obtained by CET that provide the closing relations to compute the transport properties and the collision integrals used for this study.

2.3.1 VHS Collision Integral Model

This study uses the analytical expression [19] of the Variable Hard Sphere (VHS) collision integrals Q_{ij}, given by Eq. 2.19, to ensure model consistency between CFD and the DSMC codes for future comparison.

$$\begin{aligned}
Q^{(1,1)}_{ij[VHS]} &= \frac{1}{2}\left(\frac{5}{2}-\omega_{ij}\right) f_{ij}(T) \\
Q^{(1,2)}_{ij[VHS]} &= \frac{1}{6}\left(\frac{5}{2}-\omega_{ij}\right)\left(\frac{7}{2}-\omega_{ij}\right) f_{ij}(T) \\
Q^{(1,3)}_{ij[VHS]} &= \frac{1}{24}\left(\frac{5}{2}-\omega_{ij}\right)\left(\frac{7}{2}-\omega_{ij}\right)\left(\frac{9}{2}-\omega_{ij}\right) f_{ij}(T) \\
Q^{(2,2)}_{ij[VHS]} &= \frac{1}{6}\left(\frac{5}{2}-\omega_{ij}\right)\left(\frac{7}{2}-\omega_{ij}\right) f_{ij}(T)
\end{aligned} \tag{2.19}$$

where $f_{ij}(T)$ is a factor defined as $f_{ij}(T) = \pi d^2_{\mathrm{ref},ij}\left(\frac{T}{T_{\mathrm{ref}}}\right)^{1/2-\omega_{ij}}$, T is the gas temperature, $T_{\mathrm{ref}} =$ 273 K is the reference temperature, and $d_{\mathrm{ref},ij}$ and ω_{ij} are species-pair-specific model parameters.

The VHS collision cross-section model is the most widely used DSMC model for elastic collisions [15]. It represents particles as hard spheres with a fixed diameter, assumes isotropic scattering of the hard spheres, and considers a more realistic diameter variation with the collision pair's relative speed.

2.3.2 Mass Diffusion Flux

The diffusion velocities $\mathbf{v}^D_s = \mathbf{j}_s/\rho_s$ can be expressed as the solution of the Stefan Maxwell equations constrained by mass conservation, given by:

$$\sum_{p\in S} G^D_{sp}\mathbf{v}^D_s = -\mathbf{d}^D_s \qquad \text{where } \sum_{s\in S}\rho_s\mathbf{v}^D_s = 0 \quad \forall s \in S. \tag{2.20}$$

Here, G^D_{sp} are the entries of the Stefan-Maxwell matrix in the first-order Laguerre-Sonine approximation, described in Appendix B. They are a function of the binary diffusion coefficients $\mathcal{D}_{sp}$ [20], which depend on the collision integral $Q^{(1,1)}_{ij}$ from Eq. 2.19. The diffusion driving force $\mathbf{d}^D_s$ is described by Equation 2.21 [21]:

$$\mathbf{d}^D_s = \nabla X_s + (X_s - Y_s)\,\nabla(\ln P) + \chi_s \nabla(\ln T). \tag{2.21}$$

The first term is Fick's diffusion contribution, and the second and the last are two additional diffusion contributions due to pressure and temperature gradients. The latter term is known as the Soret term or thermal diffusion. It is a function of new transport properties called thermal diffusion ratios χ_s.

They are a function of the collision integrals $Q_{ij}^{(1,1)}$ and $Q_{ij}^{(1,2)}$, as shown in Eq. 2.22.

$$\chi_s = \frac{5}{2}\sum_{p\in S}\Lambda_{sp}^{01}\alpha_p^{\kappa} \qquad \text{with } s \in S. \tag{2.22}$$

Λ_{sp}^{01} is the thermal diffusion matrix defined in Appendix B, and α_s^{κ} is the solution vector of the linear system for the thermal conductivity, defined in Eq. 2.26.

2.3.3 Viscous Stress Tensor

The viscous stress tensor from the second equation in Eq. 2.6 is a function of the transport coefficient called viscosity μ. It is obtained from the solution of the linear system:

$$\sum_{p\in S} G_{sp}^{\mu}\alpha_p^{\mu} = x_s^{\mu} \qquad \rightarrow \qquad \mu = \sum_{p\in S}\alpha_p^{\mu}x_p^{\mu} \qquad s \in S, \tag{2.23}$$

where G_{sp}^{μ} is the viscosity transport matrix and is a function of the collision integrals $Q_{ij}^{(1,1)}$ and $Q_{ij}^{(2,2)}$, as shown in Appendix B.

For monatomic gas, Equation 2.23 reduces to the Equation 2.24, as shown in [21]. The reference value $\mu_{\text{ref}}^{\text{VHS}}$ depends on parameters based on the chosen cross-section and the species mass, and ω is the viscosity exponent associated to the chosen species.

$$\mu^{\text{VHS}} = \mu_{\text{ref}}^{\text{VHS}}\left(\frac{T}{T_{\text{ref}}}\right)^{\omega}. \tag{2.24}$$

2.3.4 Heat Flux

In the last equation of Eq. 2.6, the diffusive flux tensor for the energy conservation equation is composed of two contributions: a term depending on the viscosity stress tensor and the heat flux. The latter is given by the following equation:

$$\mathbf{q} = -\kappa\nabla_x T + \sum_{s\in S} h_s\rho_s\mathbf{v}_s^D + P\sum_{s\in S}\chi_s\mathbf{v}_s^D. \tag{2.25}$$

The first term in Eq. 2.25 is the Fourier term, representing energy transport due to thermal conduction. As explained previously for the other transport properties, the translational thermal conductivity κ is also derived from the transport system in the second-order Laguerre-Sonine approximation.

$$\sum_{p\in S} G_{sp}^{\kappa}\alpha_p^{\kappa} = x_s^{\kappa} \qquad \rightarrow \qquad \kappa = \sum_{p\in S}\alpha_p^{\kappa}x_p^{\kappa} \qquad s \in S. \tag{2.26}$$

In Eq. 2.26, G_{sp}^{κ} is the thermal conductivity transport matrix, defined in Appendix B.

The second term, in Eq. 2.25, represents the diffusion of enthalpy and is a function of the diffusion velocities. Thus, including the Soret term and the pressure diffusion in Eq. 2.21 means that the second term in Eq. 2.25 contains the energy transport due to mass, pressure, and thermal diffusion. Finally, the last term in Eq. 2.25 refers to the heat flux due to species concentration gradients. It is known as the Dufour term.

For monatomic gas, Equation 2.26 reduces to the Equation 2.27, as shown in [21]. Here, k is the Boltzmann's constant and m is the species mass.

$$\kappa^{\mathrm{VHS}} = \frac{15}{4}\left(\frac{k}{m}\right)\mu^{\mathrm{VHS}}. \tag{2.27}$$

2.4 Concluding Remarks

Chapter 2 describes the mathematical equations and physical models used to simulate and analyze these flows. The chapter starts with the Navier-Stokes equations and explains the available model for the transport properties and the chemistry models. We continue with an introduction to DSMC and its features and requirements, highlighting why we use it as a reference system. Chapter 2 concludes with a detailed description of the transport model derived from the Chapman-Enskog theory, obtaining a molecular representation of the transport properties. Now, we can proceed to the next chapter, where we illustrate the chosen test cases for this dissertation and the reasoning behind these choices. A characterization of the geometries, grids, and initial and boundary conditions is provided.

Chapter 3

Test Cases

Chapter 3 gathers the details of the geometries, grids, as well as the initial and boundary conditions for the test cases being investigated in this dissertation. The chapter is divided into two sections. The first part focuses on one-dimensional problems based on the Fourier and Couette flows. We have chosen these two benchmark test cases to validate the transport models in simple test cases and compare the DSMC and the CFD solvers to assess the differences in the near continuum limit. The second part of the chapter is dedicated to two-dimensional problems. We solve a shear flow and different multi-species flows around three different blunt bodies (a cylinder, a sphere, and a sphere cone). These test cases allowed us to simulate geometry and conditions closer to reality, and further explore the effects of the transport processes modeling on the flow features and shock structure.

3.1 One-dimensional Problems

The Fourier heat transfer and the Couette flow are one-dimensional benchmark problems with well-

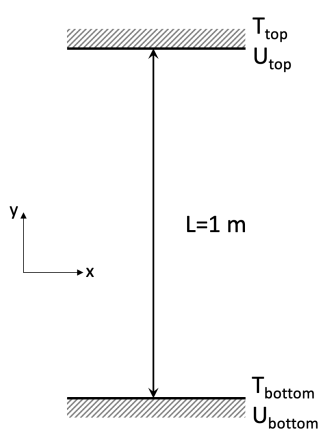

Figure 3.1: A schematic diagram of the geometry for the one-dimensional problems

documented analytical solutions. Bird [15], followed by others [22], have shown that these problems provide fundamental test cases to measure the sensitivity of the CFD code to the transport property models and to ascertain the model consistency between the CFD and the DSMC codes.

The Fourier and Couette flow present the same geometry, shown in Figure 3.1. In the Fourier heat flow problem, gas passes through two steady walls being set at different temperatures, thereby generating a temperature gradient in the flow. The Couette flow presents the walls set at the same temperature, where the bottom wall moves at constant speed in the positive x-direction relative to the upper wall. In this case, a velocity gradient is generated within the flow, causing a temperature gradient due to the heat generated by viscous dissipation.

The two problems are solved in the continuum limit. An analytical solution exists for these configurations. We set the initial conditions gathered in Table 3.1. The walls are set to be infinitely

Table 3.1: Summary of the initial conditions for the Fourier and Couette test cases

Initial conditions	Fourier Problem	Couette Problem
T_{top} [K]	600	300
T_{bottom} [K]	300	300
U_{top} [$\text{km}\,\text{s}^{-1}$]	0	0
U_{bottom} [$\text{km}\,\text{s}^{-1}$]	0	1
T_∞ [K]	300	300
ρ_∞ [$\text{kg}\,\text{m}^{-3}$]	1.003×10^{-4}	1.003×10^{-4}
Gas mixture	Monatomic Argon	Monatomic Argon

large in the x- and z-directions to ensure we solve a pure one-dimensional problem. For the Fourier flow, we impose an isothermal no-slip boundary condition at the walls and different temperatures, $T_{\text{top}} = 600\,\text{K}$ and $T_{\text{bottom}} = 300\,\text{K}$.

For the Couette flow, the bottom wall is characterized by a bulk velocity of $U_{\text{bottom}} = 1\,\text{km}\,\text{s}^{-1}$ in the positive x-direction. In contrast, both walls have no velocity imposed in the Fourier problem. Since a velocity gradient is now present in the volume domain, a supersonic outflow boundary condition must be imposed on the right side of the domain to allow the flow to move. The free stream conditions were derived directly from the relationship between the mean free path and the Knudsen number, as shown in Section **??**. A grid convergence study was conducted to ensure a fully resolved and converged solution. For the CFD simulations, the grid comprises 400 cells in the y-direction.

3.2 Two-dimensional Problems

We have selected the two-dimensional geometries described in this section to simulate and analyze more relevant hypersonic conditions. We have built this part of the research upon the knowledge acquired during the study of one-dimensional problems. These test cases are characterized by basic

axial symmetric geometries and significant diffusive transport regions around the shock and in the boundary layer (when present). The following section describes the details of the grid and their convergence studies, the mixtures, and the initial and boundary conditions.

3.2.1 Shear Flow

A shear flow is generated by two bordering supersonic jets that move parallel to each other at different speeds within a rectangular domain. The difference in the velocity creates a discontinuity which, in turn, generates two oblique shock waves characterized by different angles, where the slower the flow, the larger the angle.

Figure 3.2 shows a schematic diagram of the test cases. Moreover, Table 3.2 summarizes the chosen initial conditions for this problem. According to Figure 3.2, the dashed line on the left-handed side of the domain represents the point where the two flows meet. The CFD domain has been sized based on the DSMC grid requirement. In addition, a sponge layer was added to the top and bottom of the domain to ensure that no interaction between the shocks and the symmetry boundary condition was enforced at the domain walls. Therefore, we set $L_{\mathrm{x}} = 16\,\mathrm{mm}$ as the DSMC domain, $L_{\mathrm{y}} = 20\,\mathrm{mm}$ with the flow interface in the middle, and $L_{\mathrm{sponge}} = 10\,\mathrm{mm}$. We conduct a grid convergence study to guarantee that the obtained solution is well-resolved, as shown in Figure 3.3. The grids are more refined throughout in the y-direction, where steeper gradients are expected. The sponge layers are kept very coarse because their only feature is to dissipate the solution in the free stream region.

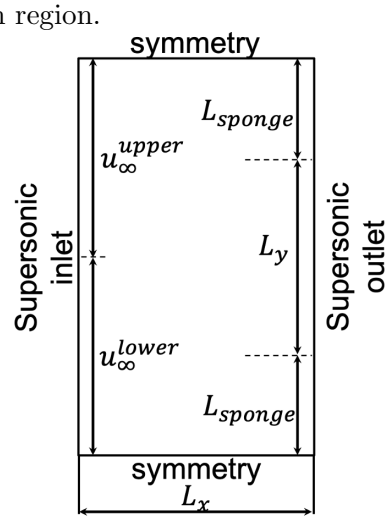

Figure 3.2: Sketch of CFD domain for the shear flow test case

Table 3.2: Free stream conditions imposed for the shear flow test case.

Free Stream Conditions	Upper Layer	Lower Layer
u_∞ [km s^{-1}]	1	3
M_∞	3.80	11.4
ρ_∞ [kg m^{-3}]	0.01	
T_∞ [K]	200	
Gas Mixture	Monatomic Gas	

Thus, starting from 200 cells along L_{y}, we increased their numbers only in that direction with an increment of 200 cells. From the shear stress and heat flux profiles in Figure 3.3, it can be noticed that the solution changes with the grid resolution until L_{y} has 600 cells or more. In this

scenario, all the flow features are well-predicted. Since there is no need to over-resolve the grid, in the end, we chose a grid size of $[L_x \times L_y] = [100 \times 600]$ cells in the region of interest and a grid size of $[L_x \times L_{sponge}] = [100 \times 14]$ cells in the sponge layer regions.

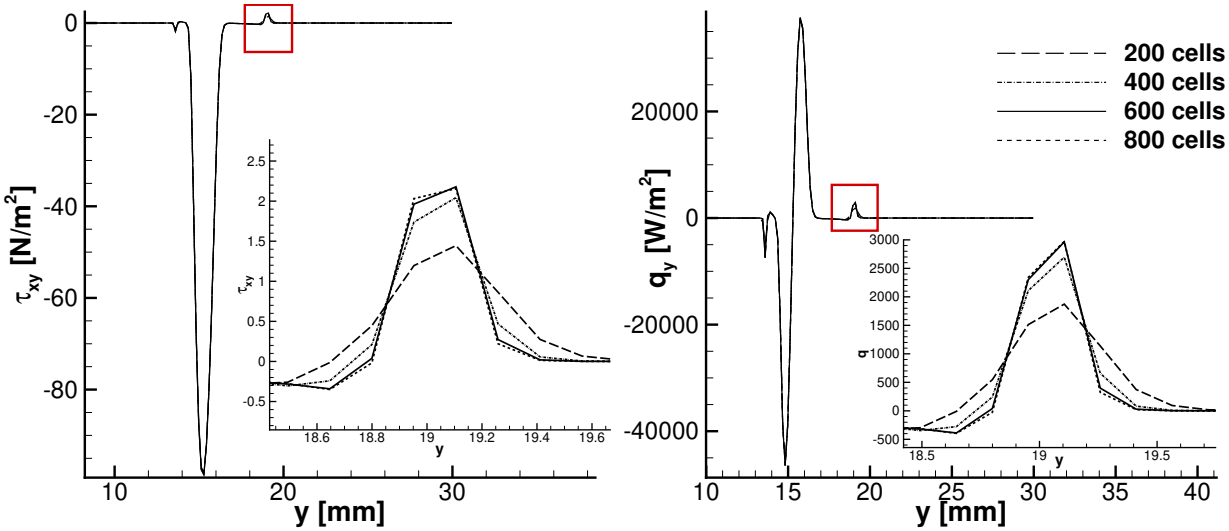

(a) Shear stress profile (b) Heat flux profile

Figure 3.3: Profiles for different grid sizes extracted at x=1 cm from the supersonic inlet. The cell number in the legend refers to the area of interest; the sponge layers are neglected.

3.2.2 Blunt Bodies

Flows around blunt bodies are the focus of the second part of this dissertation. The geometry of the blunt bodies requires simple and computationally small grids, thereby allowing us to investigate different settings and mixtures. Moreover, their shapes represent hypersonic vehicles appropriately, permitting us to examine the relevant transport phenomena occurring in more realistic conditions. A parametric study was set up as part of this dissertation to understand how the different transport properties representation affects the solutions and analyze the contributions of the different diffusive phenomena. The chosen test cases analyze flows with different mixtures, velocities, and densities over three geometries with different wall conditions. In particular, we choose a cylinder because of the replicability in DSMC and a sphere and a sphere cone because of their pertinence to hypersonic studies.

3.2.2.1 Cylinder

Figure 3.4 shows the initial geometry (pre-tailoring), the domain size, and the applied boundary conditions for the cylinder test cases by demonstrating the binary mixture setting (left-handed side)

and the air mixture (right-handed side). The cylinder radius is 0.1 m for all the problems, while the radial extent of the domain L changes with the test cases.

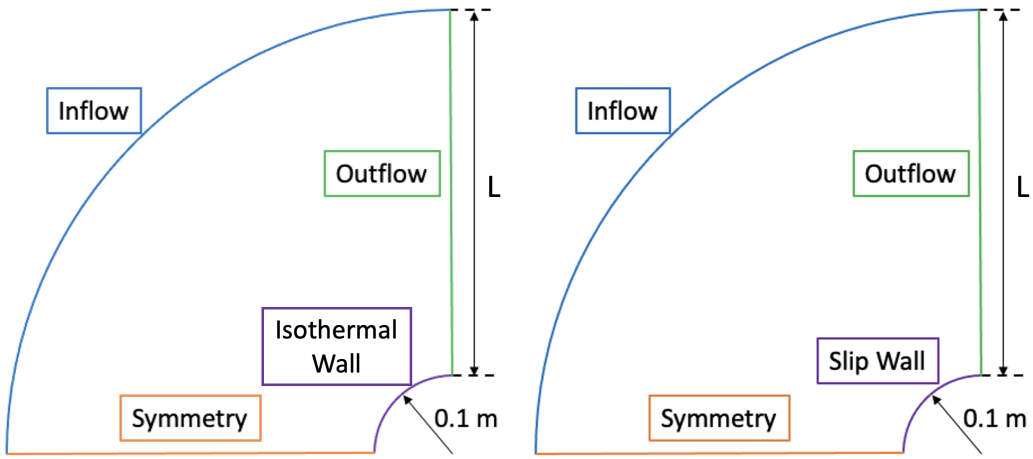

Figure 3.4: Schematic of the CFD domain for the cylinder cases

This work uses a grid representing a quarter of a cylinder of dedicated sizes. Furthermore, the grids are tailored accordingly due to the shock location and structure influenced by the free stream conditions. We conducted dedicated grid convergence studies represented in Figure 3.5. We decided to use the grid with $900 \times 200 \times 2$ points for the test cases involving the binary mixture and the grid with $900 \times 200 \times 2$ points for the air mixture cases. For the variables of interest, the maximum difference between the profiles obtained using the two most refined grids is below 1%. Table 3.3 summarized these differences.

Table 3.3: Difference between the profiles obtained with the most refined grids

Binary Mixture			Air Mixture		
Temperature	Argon Mass Fraction	Helium Mass Fraction	Temperature	N_2 Mass Fraction	O_2 Mass Fraction
0.08%	0.63%	0.28%	0.55%	0.07%	0.006%

Binary Mixture

We choose Argon and Helium as species for the binary mixture for two reasons. First, their masses differ by one order of magnitude. This difference will favor mass diffusion between species because of the dependence of the speed at which molecules travel to the temperature and the species' masses. In particular, it is known that the thermal motion of molecules is responsible for the transport of mass, momentum, and energy relative to the flow leading to diffusivity, viscosity, and thermal conductivity This motion is represented by the thermal velocity $c_{th,s} = \sqrt{\frac{3kT}{m_s}}$. Thus, at an equal temperature, lighter particles will diffuse more rapidly than heavier particles. Consequently, diffusion is favored by the species' different molecular weights be-

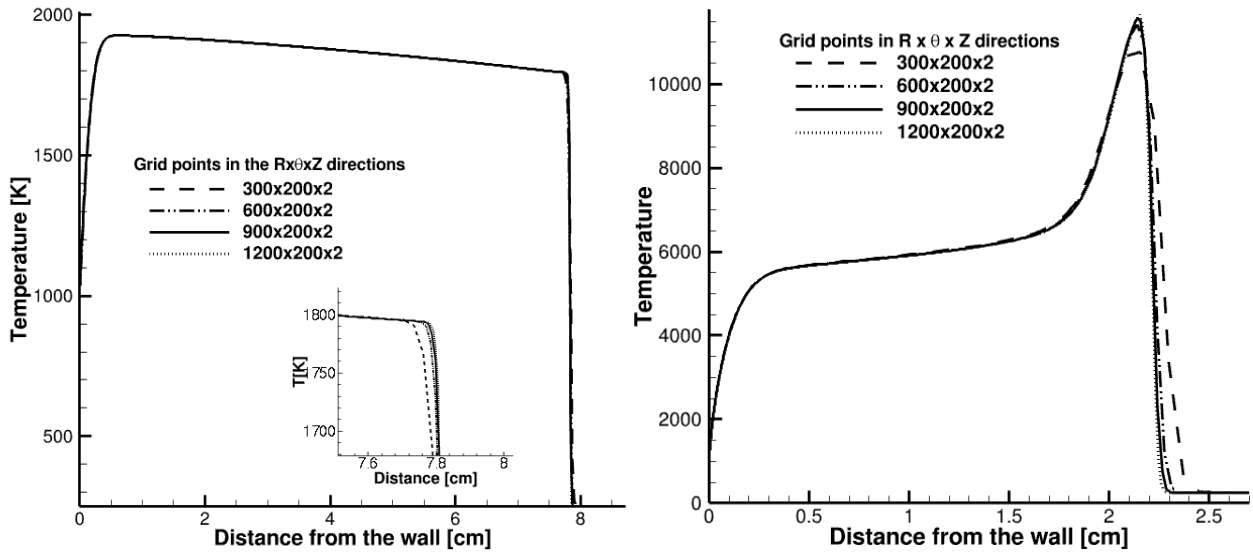

(a) Binary mixture (b) Air mixture

Figure 3.5: Temperature profiles along the stagnation line for the cylinder case, obtained by using different mixtures and different grid sizes.

cause the varying thermal speeds of the molecules result in a net movement of particles from regions of high concentration to regions of low concentration, facilitating the mixing of substances. Second, Argon and Helium are inert gasses that do not react with other chemical substances. Thus, these problems pertaining to the binary mixture will allow us to study the effects of diffusion and avoid undesirable differences due to the inconsistency between the DSMC and the CFD chemistry models. We set the initial mixture composition to 90.9% Ar + 9.1% He to have the same number of particles of both species per unit volume. The initial and the boundary conditions are summarized in Table 3.4. We study this geometry and gas mixture with two sets of initial conditions. In particular, fixing the density so that the $Kn = 10^{-3}$, we vary the velocity to replicate realistic post-shock conditions. In the same way, we fix the velocity to the most extreme case and vary the density to simulate a more dense and rarefied flow.

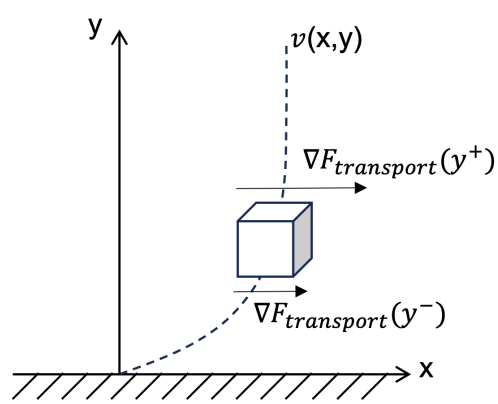

Figure 3.6: Sketch of transport phenomena in a boundary layer

Table 3.4: Initial and boundary conditions for the binary mixture test cases at a constant velocity and a constant density

Free Stream Velocity Variation	
Free Stream Temperature [K]	250
Wall Temperature [K]	1000
Wall BC	no-slip wall
Free Stream Density [$\mathrm{kg\,m^{-3}}$]	3.74×10^{-4}
Free Stream Velocities [$\mathrm{km\,s^{-1}}$]	4 6 8

Free Stream Density Variation	
Free Stream Temperature [K]	250
Wall Temperature [K]	1000
Wall BC	no-slip wall
Free Stream Velocity [$\mathrm{km\,s^{-1}}$]	8
Free Stream Densities [$\mathrm{kg\,m^{-3}}$]	1×10^{-4} 3.74×10^{-4} 1×10^{-3}

Air Mixture

The air mixture consists of five species (N_2, O_2, NO, N, O) with the initial composition of 77% N_2 and 23% O_2. These geometry and mixture have been used for comparing the solutions obtained using DSMC and CFD with different chemical and diffusion models. In the CFD simulations, the vibrational energy is approximated as a simple harmonic oscillator, and the electronic energy is neglected to be consistent with the DSMC internal energy model. Table 3.5 summarizes the selected initial and boundary conditions for these problems. The free stream density is derived from the Knudsen number being set in order to 10^{-3} to simulate the near-continuum flow regime.

Table 3.5: Different inflow conditions for the air mixture test case imposed for the comparison study

	v_∞[$\mathrm{m\,s^{-1}}$]	T_{wall}[K]	Wall BC	T_∞[K]	ρ_∞[$\mathrm{kg\,m^{-3}}$]
Free-stream velocity variation	4	1000	Non catalytic no-slip wall	250	3.74×10^{-4}
	5				
	6				

3.2.2.2 Sphere and Sphere Cone

The sphere and sphere cone are the two geometries utilized to validate the implementation of the transport model, which is based on CET. Moreover, these two geometries are used to study the diffusive effects on flows around different blunt bodies. Figure 3.7 represents the CFD domains for both geometries based on the shock-tailored grid and demonstrates the size and the applied boundary conditions. The grids comprise of $900 \times 150 \times 2$ grid points for the sphere and $1000 \times 300 \times 2$ for the sphere cone.

Table 3.6 summarizes the free stream initial conditions and the wall boundary conditions for both the sphere and sphere cone test cases. These problems were set up to conduct a detailed analysis of all the factors participating in the diffusive transport phenomena at different locations along the flow field. We examine conditions that favor steep gradients in the areas of interest,

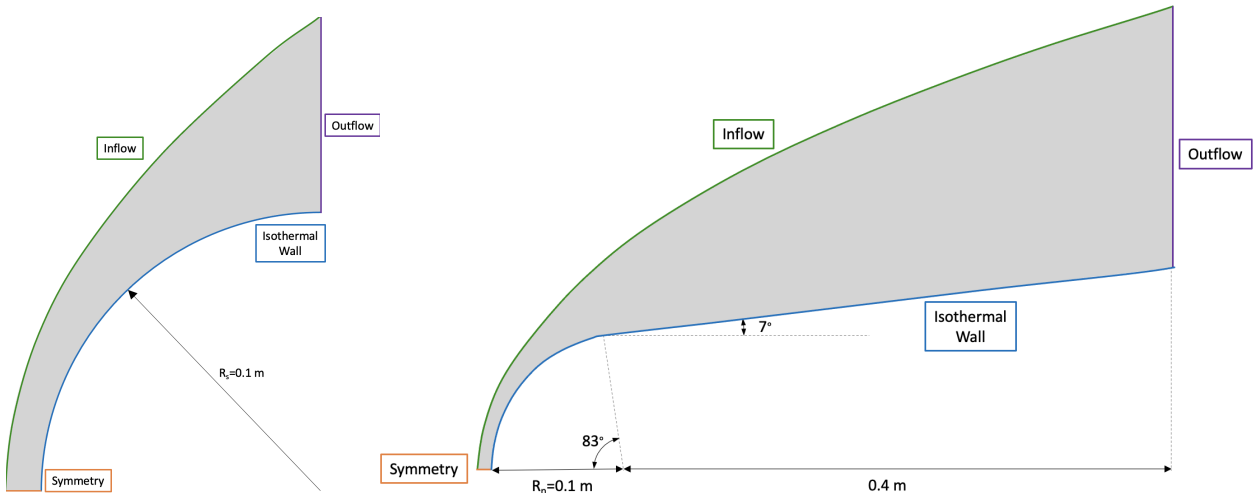

(a) Sphere test cases **(b) Sphere-cone test cases**

Figure 3.7: Schematic of the CFD domain

such as a cold and catalytic wall. In particular, we vary the catalytic efficiency from $\gamma = 0$, which corresponds to a non-catalytic wall boundary condition, to $\gamma = 1$, in which the wall is fully catalytic. Between this interval of $\gamma = [0, 1]$, we further consider three intermediate values of different orders of magnitude. The sphere-cone is a canonical yet important geometry for a hypersonic flow that

Table 3.6: Initial and boundary conditions for the sphere and sphere cone test cases

Catalytic efficiency Variation	
Free Stream Temperature	300 K
Wall Temperature	300 K
Wall BC	Isothermal wall
Free Stream Velocity	$5\,\mathrm{km\,s^{-1}}$
Free Stream Densities	$3.74 \times 10^{-4}\,\mathrm{kg\,m^{-3}}$
Catalytic efficiency γ	0, 0.005, 0.01, 0.1, 1

allows us to study the diffusion effects at different locations along the body. In this instance, we extract the solutions at the locations shown in Figure 3.8 and focus on the entropy layer and near-outflow regions. The entropy layer is a feature of the flow around blunt bodies surrounded by a highly curved oblique shock. The shock near the nose region is nearly normal. Thus, the flow in that region will undergo a much steeper change in the entropy than the flow passing through the shallower shock angle further from the body centerline. Consequently, an entropy layer is generated near the leading edge that develops downstream along the body due to the steep entropy gradient experienced by the flow.

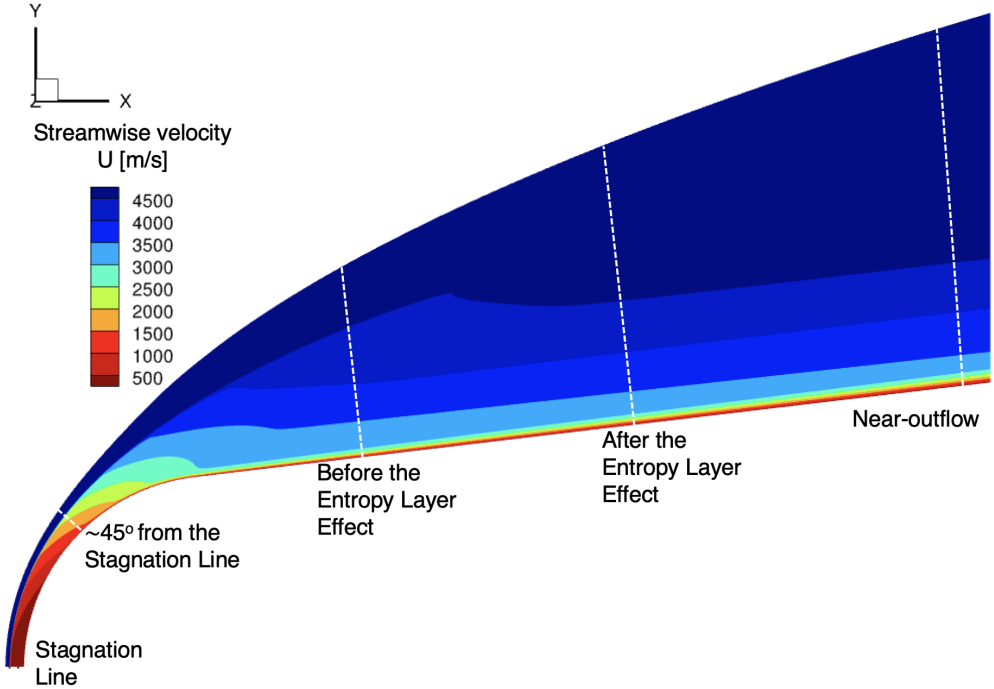

Figure 3.8: Extraction locations for the sphere-cone case.

3.3 Concluding Remarks

Chapter 3 presents the chosen test cases, which allow us to conduct a parametric study varying the main feature of the flow. We considered different geometries, mixtures, as well as initial and boundary conditions to identify an envelope of parameters where the effects of interests are significant. Subsequently, Chapter 4 is dedicated to the solutions to these problems and the relative analysis of them. We solve the problems and compare the results using the numerical models previously explained in Chapter 3.

Chapter 4

Results

Chapter 4 collects the results and their analysis for the test cases explained in the previous chapter, comparing the solution obtained using the CFD solver with different diffusion models to the DSMC solutions. The chapter starts with the test cases involving the monoatomic Argon gas. These test cases, the one-dimensional Couette and Fourier flow, the two-dimensional shear flow, and the cylinder cases, are used to validate the consistency between the codes. Then, we move toward the problem representing more realistic hypersonic conditions. Thus, we simulate and gather the solutions for blunt bodies and the different multi-species mixtures. In particular, we show the cylinder, sphere, and sphere cone results in a 5-species air mixture and conclude with the cylinder solution using a binary mixture. These test cases allow us to study the effects of the chemistry and diffusion models on the flow field in the near continuum regime. The CFD results were obtained using US3D, a code developed at the University of Minnesota, routinely used for complex hypersonic computational fluid dynamics (CFD) simulations. All the DSMC solutions were run by Michael Kroells at the University of Minnesota using MGDS, an in-house code capable of large-scale 3D Direct simulation Monte Carlo (DSMC) calculations.

4.1 Monatomic gas test cases

The Fourier and the Couette flows are two one-dimensional benchmark test cases that are solved to assess whether both the CFD and the DSMC solver produce the same results, as expected in the continuum limit. The CFD code, US3D, solves the CET formulation to solve the monatomic viscosity and thermal conductivity, expressed in Equations 2.24 and 2.27. In MGDS, the DSMC solver, we use Bird's Variable Hard Sphere (VHS) model [15] for the Argon cross-sections, using the parameters for Argon summarized in Table A.2 in Appendix A.

Figure 4.2 shows the temperature profile extracted along the centerline of the geometry in Figure 3.1 for the Fourier flow (left-handed side) and the Couette flow (right-handed side). Because of the study that preceded this work conducted by Schwartzentruber et al. [23–25] and Stephani et

al. [26–28], we expected to see near-exact agreement between the solutions. Despite the negligible differences between the two transport models, we can observe that the CFD solution with the VHS viscosity models is qualitatively almost identical to the DSMC solution. This trend can be better appreciated when we solve problems more representative of the conditions encountered in actual hypersonic flows. Thus, we solve the two-dimensional problems: the Argon flow around a cylinder and the shear flow. Figure 4.3 shows the temperature profile, extracted along the stagnation line, for an Argon flow moving around a cylinder at $5\,\mathrm{km\,s^{-1}}$ and characterized by $Kn = 10^{-3}$. The geometry for this test case is shown in the right-handed side of Figure 3.4. We compare the solutions obtained using the CFD code with different viscosity models, explained in Chapter 2 and the DSMC solver.

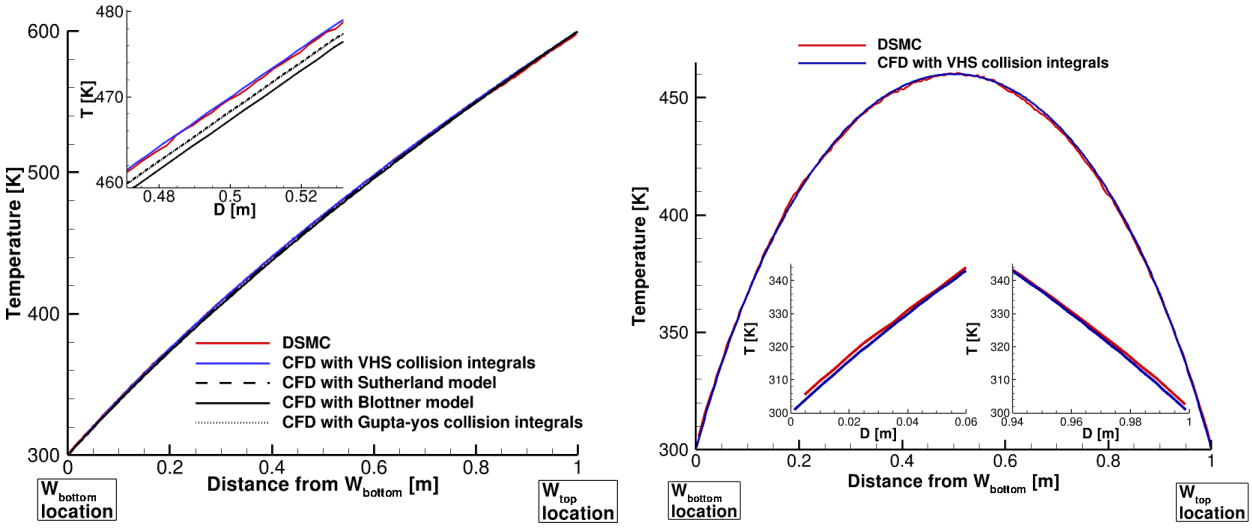

(a) Fourier flow (b) Couette flow

Figure 4.2: Extraction of the temperature profiles along the centerline in Fig. 3.1 for the one-dimensional flow problems.

The temperature and density profiles in Figure 4.3 establish that the DSMC solution predicts a thicker shock than any CFD solution. CFD and DSMC solutions agree almost entirely in the post-shock region, with a few deviations observed in the shock region due to the flow's non-continuous nature. We can observe that the differences between the CFD solution with the VHS model and DSMC solutions are smaller than the difference between the US3D viscosity models. Indeed, the CFD solution with the VHS transport model and the DSMC solution demonstrate near-exact agreement. This outcome was expected because the CFD and DSMC codes are fully consistent when we simulate problems without chemical reactions and diffusion phenomena.

The validation analysis is concluded with the two-dimensional shear flow, explained in section 3.2.1. Figure 4.4a shows the density contour plot of the CFD solution. As the schematic diagram in Figure 3.2 illustrates, the two parallel, steady supersonic jets enter the domain from the left-

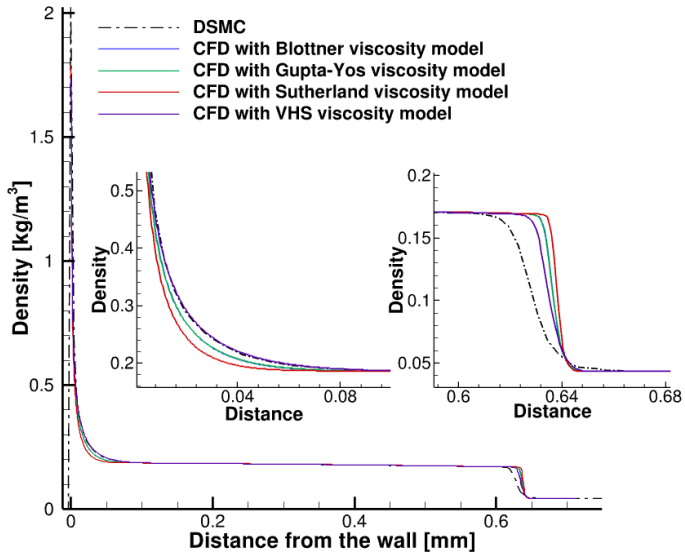

(a) Density profile

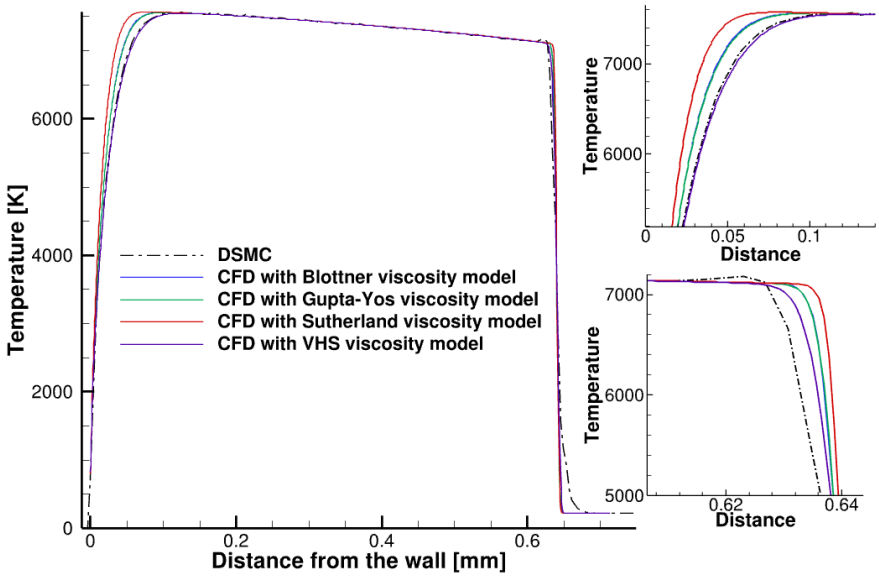

(b) Temperature profile

Figure 4.3: Comparison of the solutions extracted at the stagnation line for the Argon flow around a cylinder, and obtained using DSMC and CFD with different diffusion viscosity models.

handed side at different speeds and exit from the right-handed side. The density plot in Figure 4.4a highlights the two oblique shocks initiated at the merging point and their features, such as the angle and the shock front. The temperature contour in Figure 4.4b displays the shear region where the steepest temperature gradients are located. As validation and proof of concept, we verify that the flow in the data extraction location is in the near continuum regime, and we are far enough

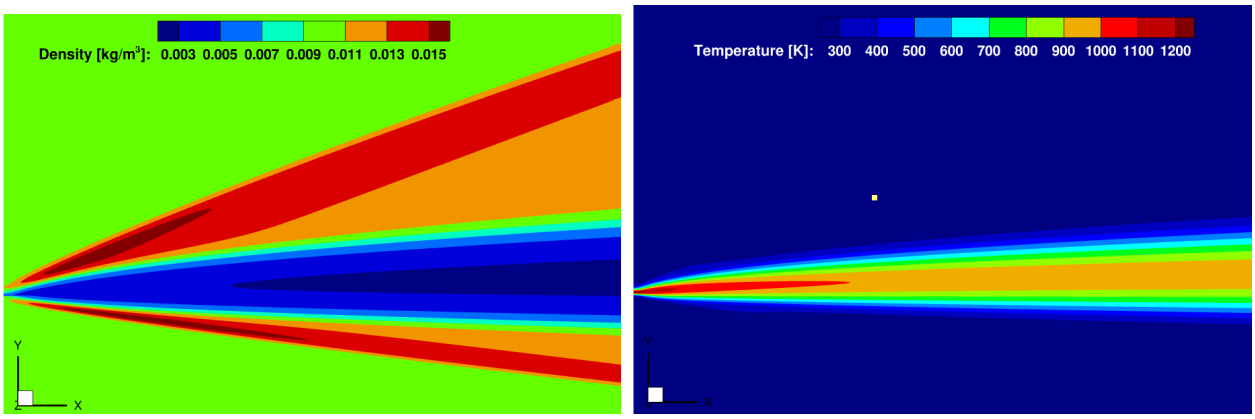

(a) Density contour plot **(b) Temperature contour plot**

Figure 4.4: CFD solution of the two-dimensional shear flow problem

from the velocity discontinuity (where the two flows meet). Thus, we evaluate the gradient-length Knudsen number, as defined in Equation 1.2, and its flow field distribution for this problem is shown in Figure 4.5. As expected, the regions close to the discontinuity are characterized by the high values of Kn_{GL}. As we move downstream, Kn_{GL} decreases. In particular, the downstream region coinciding with the extraction location marked in Figure 4.5 is characterized by a $Kn_{\mathrm{GL}} \approx \mathcal{O}(10^{-3})$ or smaller when moving away from the centerline.

In Figure 4.6, we compare the density profiles for the DSMC solution with the CFD solution obtained with the VHS transport model extra. While we solved the shear flow using CFD with the built-in transport models, their comparisons confirm what was observed previously in the cylinder and the one-dimensional problems. Thus, we omitted it in the plot for clarity. The comparison between the DSMC and the CFD solutions in Figure 4.6 demonstrates a good qualitative agreement between both results, as expected due to the consistency between codes. However, the DSMC solution predicts a slightly more acute angle for the oblique shock wave angle on the upper half of the domain than in the CFD result. Based on the work conducted by Schwartzentruber et al. [24], where they studied a flow over a Hollow-Cylinder-Flare Geometry in hypersonic condition, we can deduct that the differences are mainly due to the initial slip region. They observed that the leading edge shock predicted by the Navier-Stokes equations is further from the surface than the equivalent DSMC solutions. Thus, they showed that the reason for the differences lies behind the fact that the CFD uses a no-slip boundary condition, whereas the DSMC naturally allows for velocity slip. Consequently, we decide to focus on blunt bodies for the rest of the study. The boundary conditions for this geometry can be set consistently in both the CFD and the DSMC code.

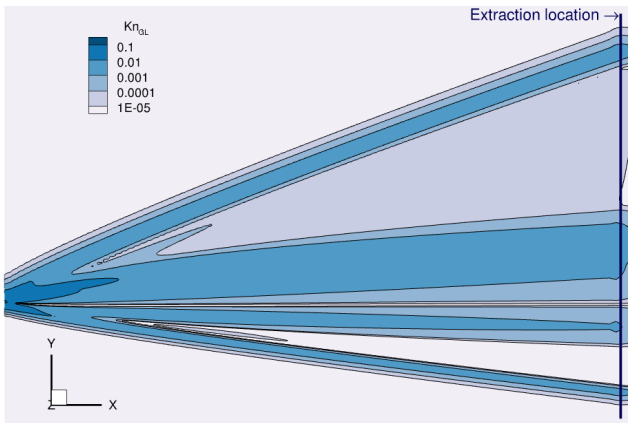

Figure 4.5: Gradient-length Knudsen number distribution in the CFD flow field

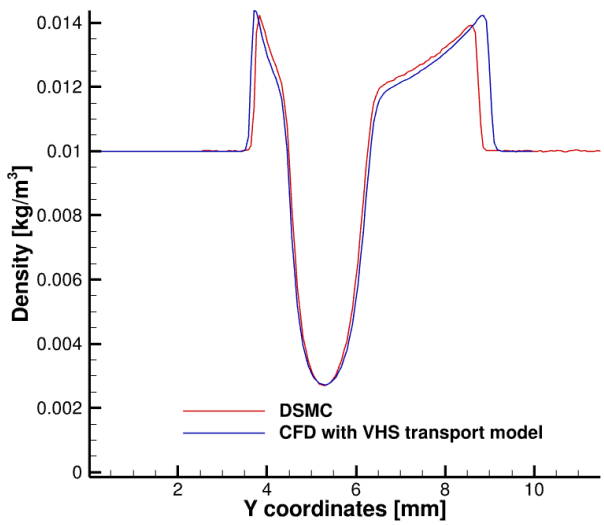

Figure 4.6: Sketch of CFD domain for the shear flow test case

4.2 Multi-Species Mixture

As described in Chapter 3, the second part of the results are dedicated to flows around blunt bodies in multi-species mixture. First, we analyze the effect of the chemistry and diffusion models on the cylinder test cases in the 5-species airflow. Second, we repeated the analysis using a binary non-reacting mixture to mitigate the differences in the comparison caused by the different chemistry models used in the DSMC and the CFD codes. Finally, we used a sphere and a sphere cone to investigate how the effect of the diffusion model changes with geometry, wall boundary condition, and location in the flow field.

4.2.1 Cylinder

In this section, we gather the solutions of the flows around a two-dimensional cylinder in the near-continuum regime described in Section 3.2.2.1.

The analysis starts with the simulations of a two-dimensional hypersonic flow over a cylinder in a five-species air mixture at the near-continuum regime. We study the effect of the chemical kinetics by comparing the Park model and the Modified Marrone-Treanor chemical kinetics model, available in US3D (CFD code), and the total collision energy model, available in MGDS (DSMC code). For all the CFD simulations, we use the SCEBD approximation [2] to model diffusion, and the transport properties are based on the Gupta-Yos collision integrals [4], described in Section 2.1.1.1 and 2.1.1.2, respectively. The setup and the initial and boundary conditions for this problem are summarized in Table 3.5.

Figures 4.7, 4.8, and 4.9 represent the plots of the species mass fractions extracted at the stagnation line with respect to the distance from the cylinder wall. The wall is located at zero on the x-axis, while the shock is located in the CFD solutions around 2.8 cm, 2.2 cm, and 1.8 cm for the 4km/s, 5km/s, and 6km/s, respectively. The differences in the results are expected because neither the transport nor the chemistry models are consistent between the DSMC and the CFD code. However, a closer look at how the rates and vibrational favoring are defined in the different chemistry models can explain the behavior in the post-shock and near-wall regions.

While the TCE model does not explicitly account for vibrationally favored dissociation, Park's model considers this phenomenon by utilizing the geometric mean of translational and vibrational temperature. This approach enables dissociation reactions only when the vibrational temperature reaches a significant threshold, thus capturing the essence of vibrational favoring in the calculation of reaction rates. This discrepancy between these chemistry models entails that dissociation begins to occur in the DSMC simulation as soon as the translational temperature increases within the bow shock. In contrast, simulations performed with the Park model begin to dissociate once the vibrational temperature begins to increase. Therefore, dissociation in CFD with the Park model is delayed with respect to the dissociation predicted using DSMC, as shown in the molecular species profile in Figures 4.7, 4.8, and 4.9.

Furthermore, as explained in Section 2.1.2.2, the MMT model presents a lower effective oxygen dissociation rate respecting the Park model. In fact, Figure 4.7 shows that the O_2 dissociation predicted by the MMT model is slower than the Park model. Consequently, the O_2 mass fraction at the wall predicted with the MMT model is higher than the one predicted by the Park model. Furthermore, the lower degree of dissociation in MMT results in a higher post-shock temperature and larger shock stand-off. However, comparing the solutions at the different free-stream velocity increases, we notice that these differences become less pronounced for higher Mach numbers flow because the rate of oxygen dissociation also increases. Hence, the MMT and Park models agree very well in terms of post-shock density and temperature (translational and vibrational), as well as species concentration for the case characterized by the highest velocity. Figure 4.9 shows that all the considered chemical kinetics predict a nearly complete dissociation of O_2 in the post-shock region.

If we analyze now the region near the cylinder surface, we can observe remarkable differences between the CFD and DSMC results. All the test cases in Figures 4.7-4.9 present a spike in the mass fraction molecular species, mainly N_2, and a related decrease in the atomic species, mainly O. Furthermore, the magnitude of these differences increases with free-stream velocity. To understand the reasons behind this trend, we investigate possible causes.

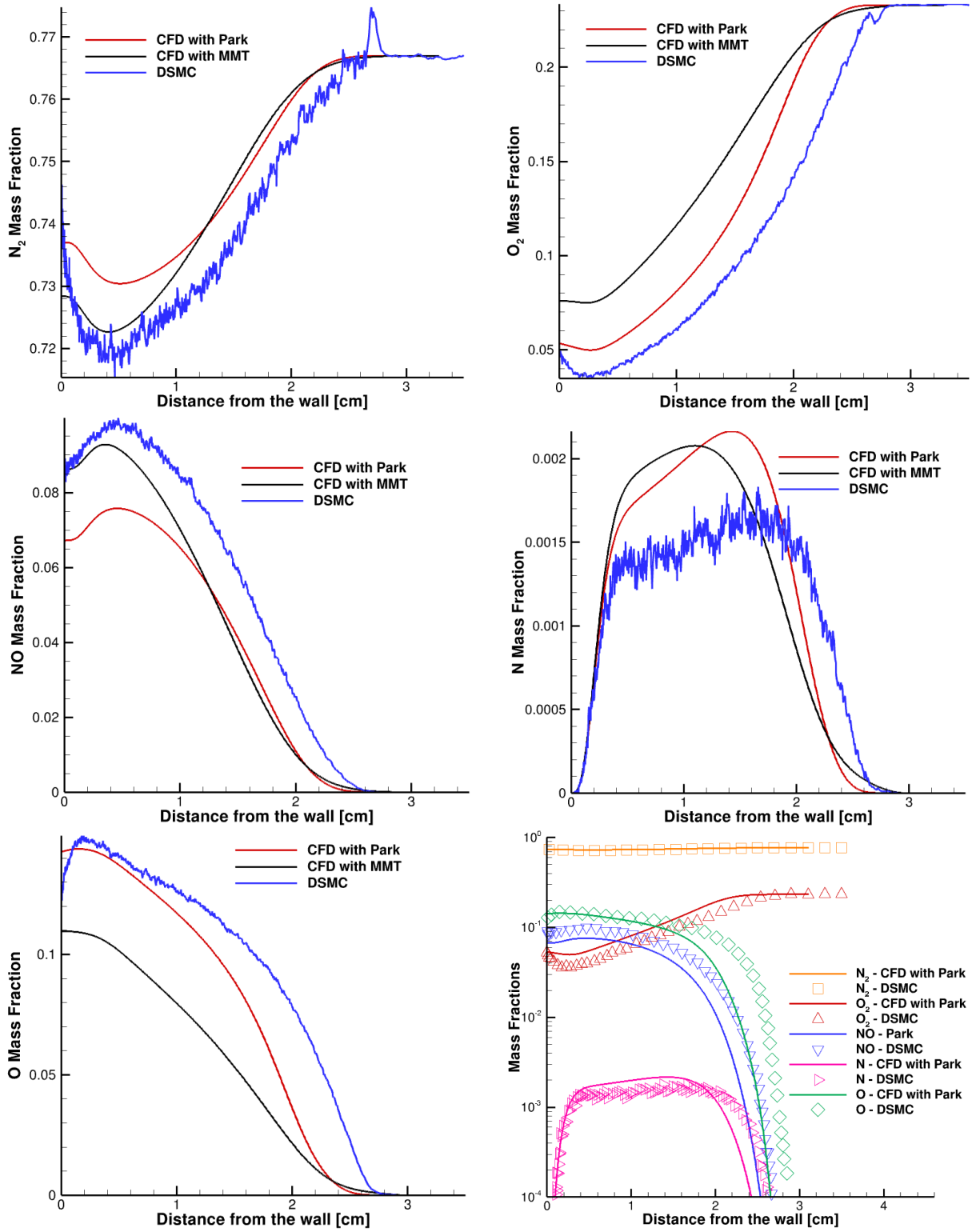

Figure 4.7: Mass fraction profiles comparison of MDGS and US3D solutions for the $4\,\mathrm{km\,s^{-1}}$ airflow around a cylinder case, extracted on the stagnation line and obtained with different chemical kinetics

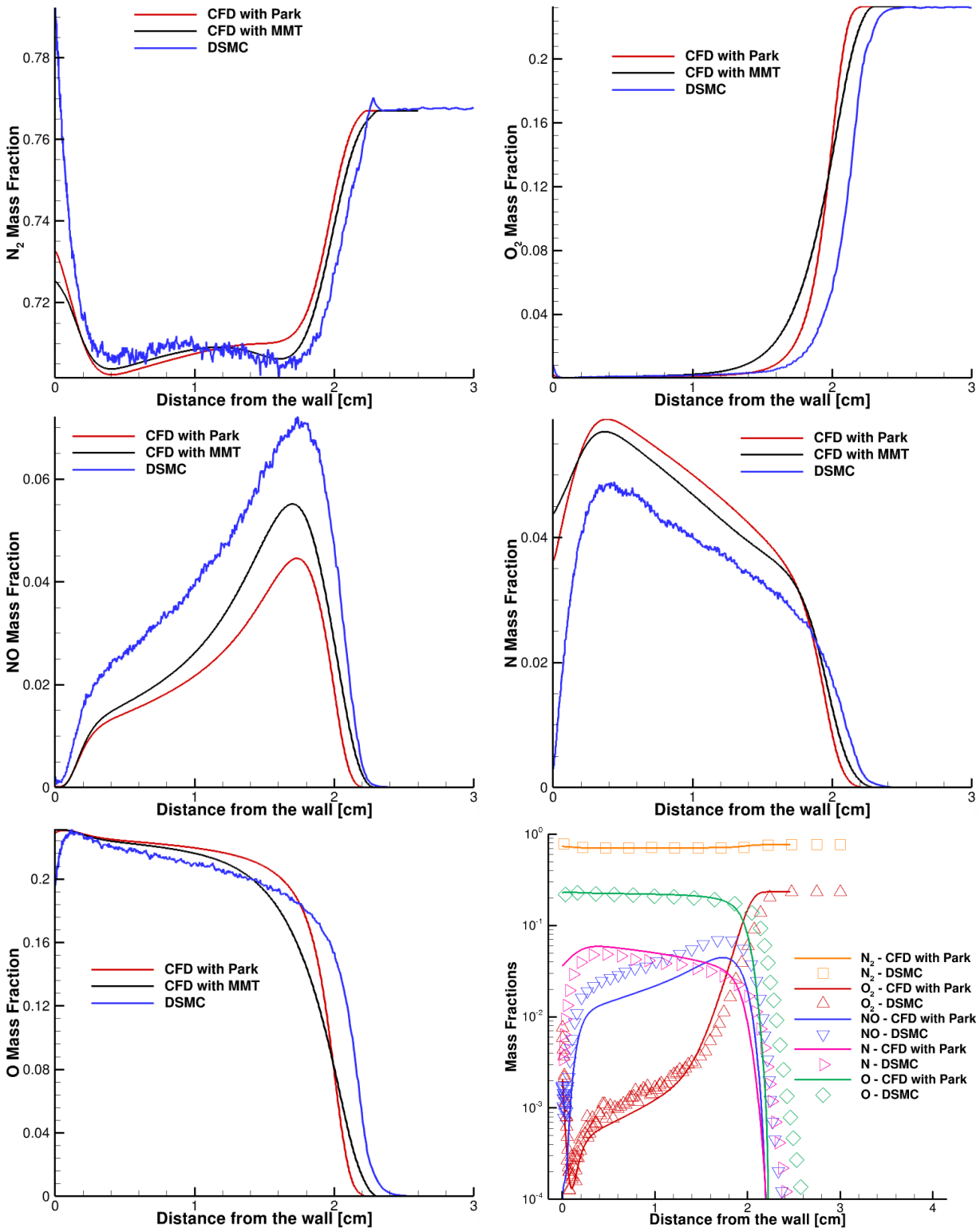

Figure 4.8: Mass fraction profiles comparison of MDGS and US3D solutions for the $5\,\mathrm{km\,s^{-1}}$ airflow around a cylinder case, extracted on the stagnation line and obtained with different chemical kinetics

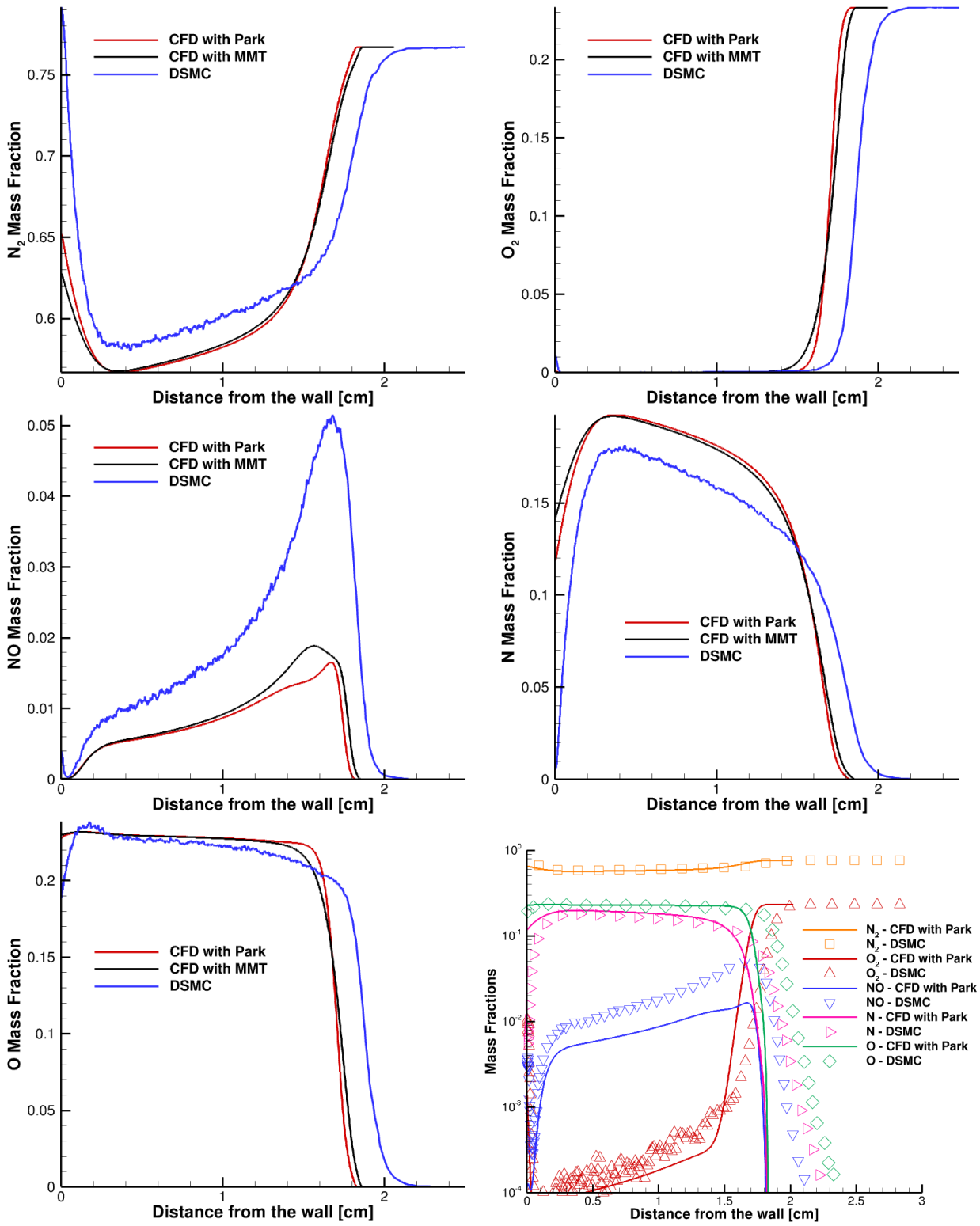

Figure 4.9: Mass fraction profiles comparison of MDGS and US3D solutions for the $6\,\mathrm{km\,s^{-1}}$ airflow around a cylinder case, extracted on the stagnation line and obtained with different chemical kinetics

First, we ruled out recombination by rerunning these cases in DSMC without recombination, showing a negligible effect on the mass fractions. Second, we investigate the diffusion effect since the N_2 mass fraction surpasses the free-stream value in the near-wall region for the $6\,\mathrm{km\,s^{-1}}$ case.

Initially, we extended the transport models available in US3D by coupling it with an open-source library developed at the von Karman Institute for Fluid Dynamics, MUTATION++ [29] (MUlticomponent Thermodynamic And Transport properties for IONized gases). MUTATION++ provides a repository for thermodynamic, transport, chemistry, and energy transfer properties associated with non-equilibrium plasma flows, allowing us to replicate the results using the Stefan-Maxwell equations to solve the multi-component diffusion. However, the diffusion model offered by the coupled US3D-MUTATION++ code does not take into account the additional transport property and diffusion terms derived from the CET (Sec. 2.3) because they are considered negligible, based on the knowledge acquired from the literature. We found negligible differences in the solution at these conditions, as shown in Figure 4.10.

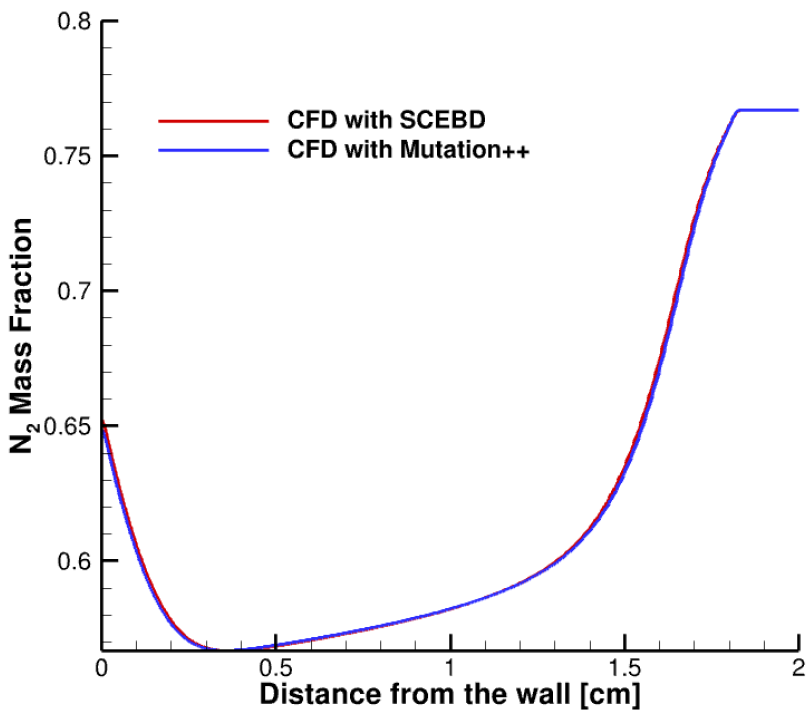

Figure 4.10: N2 mass fraction profiles comparison of the 6 km/s flow around a cylinder using different diffusion models on the stagnation line.

Besides the chemical kinetics models, the diffusion fluxes definition is the main difference between the codes. We want to estimate the magnitude of the additional diffusion terms derived from the Chapman-Enskog theory. Recalling Equation 2.21, they defined the mass diffusion driving force as a superimposition of the Fickian contribution, the Soret term depending on the temperature, and the pressure diffusion term. Hence, we extract the thermal diffusion coefficient $\chi_{T_{N_2}}$ of N_2

from the DSMC solution, and the log temperature $\nabla \ln T$ and the N_2 mass fraction gradients from the CFD solution. In Figure 4.11, we compared the different diffusion contributions on the left y-axis, superimposed to the CFD and DSMC N_2 mass fraction on the right y-axis in the near-wall region. In particular, the solid black line represents the Fickian diffusion (first term in Eq. 2.21), the dashed black line represents the Soret term (second term in Eq. 2.21), the red line is the CFD solution and the blue line is the DSMC solution.

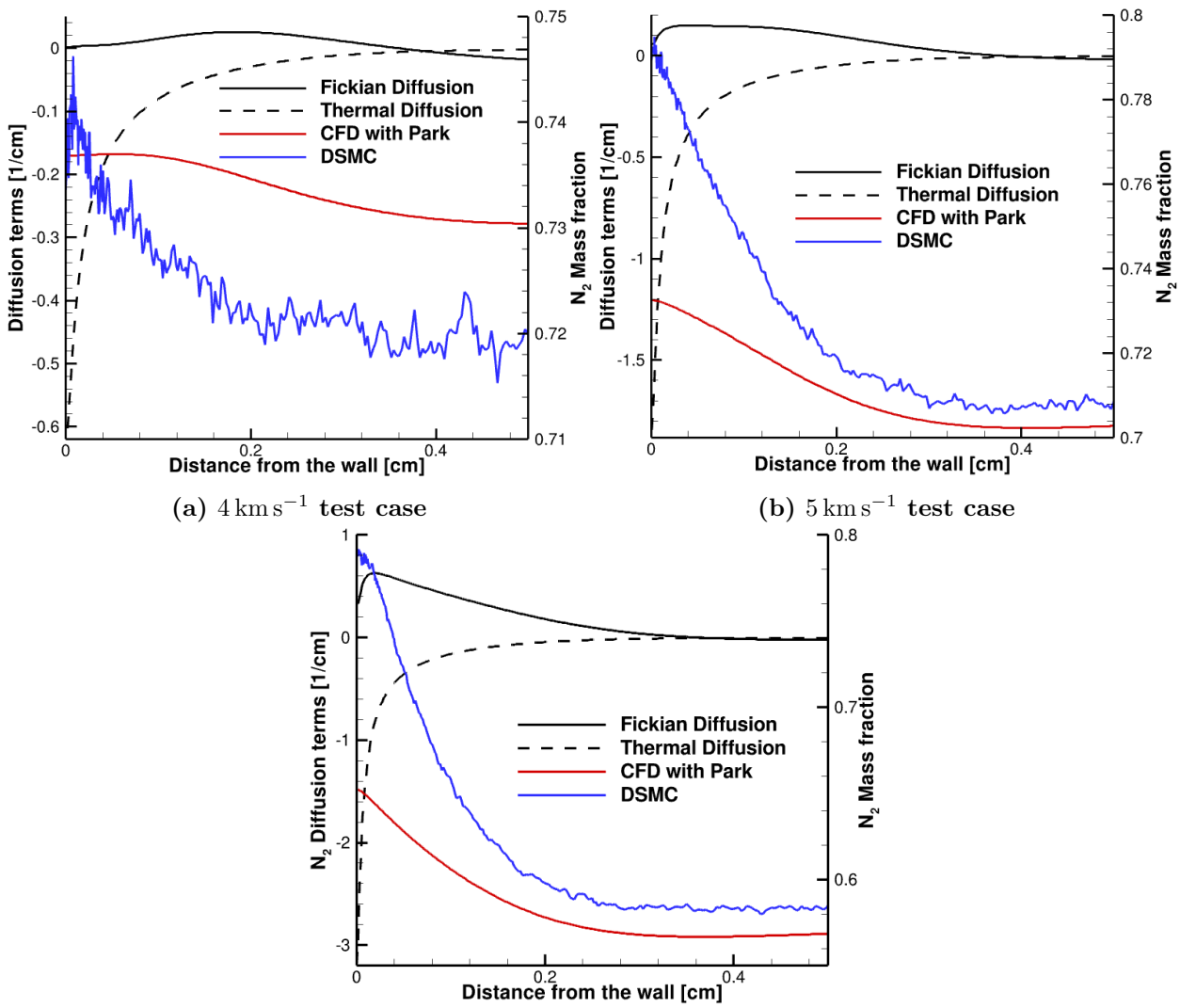

(a) $4\,\mathrm{km\,s^{-1}}$ test case

(b) $5\,\mathrm{km\,s^{-1}}$ test case

(c) $6\,\mathrm{km\,s^{-1}}$ test case

Figure 4.11: Comparison of the diffusion contribution and mass fractions of N_2 for airflow around a cylinder at different free-stream velocities

These figures display that thermal diffusion overtakes mass diffusion in the near-wall, and the N_2 mass fraction predicted by DSMC increases when thermal diffusion becomes the dominant

effect. Furthermore, the thermal diffusion term at the wall increases with the free stream velocity in conjunction with the discrepancy in the mass fraction becoming more significant with the free stream with the flow velocity. While these results are in opposition to the assumption of these terms being negligible, similar effects were observed by Holman et al. [30]. They observed less evident effects because they simulated a flow with a higher free-stream velocity and wall temperature.

Thus, we implement in US3D the full diffusion model derived from CET, described in Section 2.3 and Appendix C to quantify the effects that these additional diffusion terms have on the flow field and how they are affected by the problem conditions. In this model, the mass diffusion flux is characterized as the combination of diffusion as a consequence of mole fraction gradients (Fickian term), temperature gradient effects (Soret term), and pressure gradient effects. Additionally, the heat flux includes an extra component (Dufour term) that accounts for the contribution of species mole fractions to energy transport. Figures 4.12, 4.13, and 4.14 show the mass fraction profiles extracted at the stagnation line for the $4\,\mathrm{km\,s^{-1}}$, $5\,\mathrm{km\,s^{-1}}$, and $6\,\mathrm{km\,s^{-1}}$ cases, respectively. These plots illustrate a comparison between three different solutions. The red lines represent the DSMC solution; the blue and black lines correspond to the CFD solution obtained using the SCEBD and full diffusion models derived from the Chapman-Enskog analysis, respectively. It is important to note that the SCEBD model exclusively considers the Fickian diffusion term. The significant effect on the discrepancy in the comparison is due to the different chemistry models, as explained previously in this section. However, distinctive and noteworthy differences at the shock location and in the near-wall region can be noticed between the CFD and the DSMC results.

In the shock region of the $4\,\mathrm{km\,s^{-1}}$ and $5\,\mathrm{km\,s^{-1}}$ solution, located approximately 2.8 cm and 2.2 cm from the wall, respectively, the CFD solution with the diffusion model based on CET reproduces the distinctive features present in the DSMC solution. In particular, in Figures 4.12 and 4.13, we observe that the CFD solution with the full diffusion model shows the observed bump in the N_2 mass fraction profiles and the dent in the O_2 mass fraction profiles, in agreement with the DSMC simulation. In the near-wall region, from a qualitative perspective, the CFD solution using the diffusion model derived from CET is in closer agreement with the DSMC prediction than the CFD results with the SCEBD approximation. In particular, Figures 4.13 and 4.14 show almost a perfect agreement between the O mass fraction profile obtained by solving the Chapman-Enskog theory in the CFD solver and the DSMC solution at the wall. Moreover, as shown in Figure 4.12, at a lower speed, while the magnitude of the CFD solution with the SCEBD model agrees with the DSMC solution at the wall, the diffusion model derived from CET predicts results in a good qualitative agreement with the trend captured by DSMC.

While comparing the solution of the airflow around the cylinder obtained with DSMC and CFD with the diffusion model from CET showed good qualitative agreement capturing specific trends that were not captured by the SCEBD approximation, further investigations are necessary to isolate the diffusion models' effect.

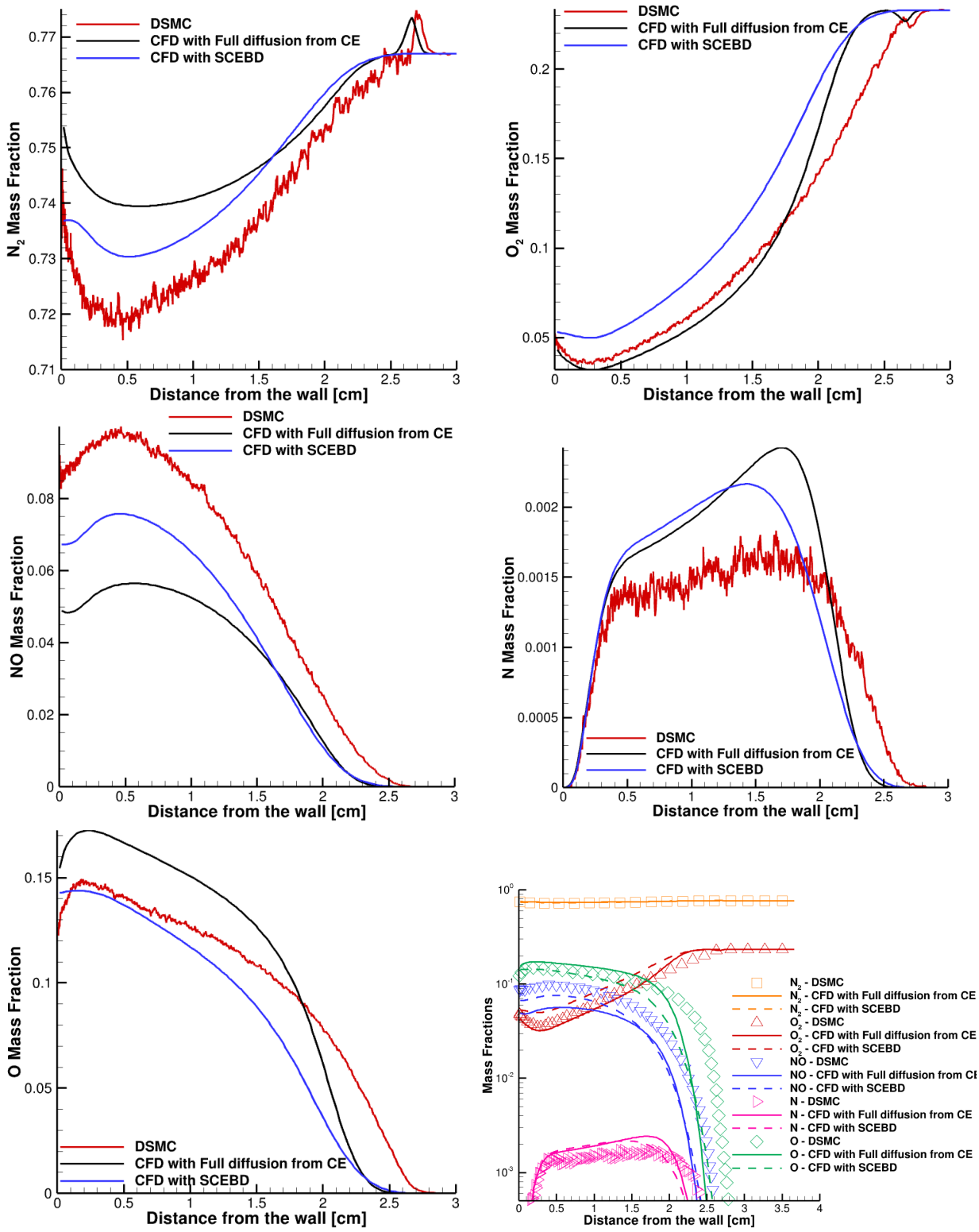

Figure 4.12: Mass fraction profiles comparison of MDGS and US3D solutions for the $4\,\mathrm{km\,s^{-1}}$ airflow around a cylinder case, extracted on the stagnation line and obtained with different diffusion models

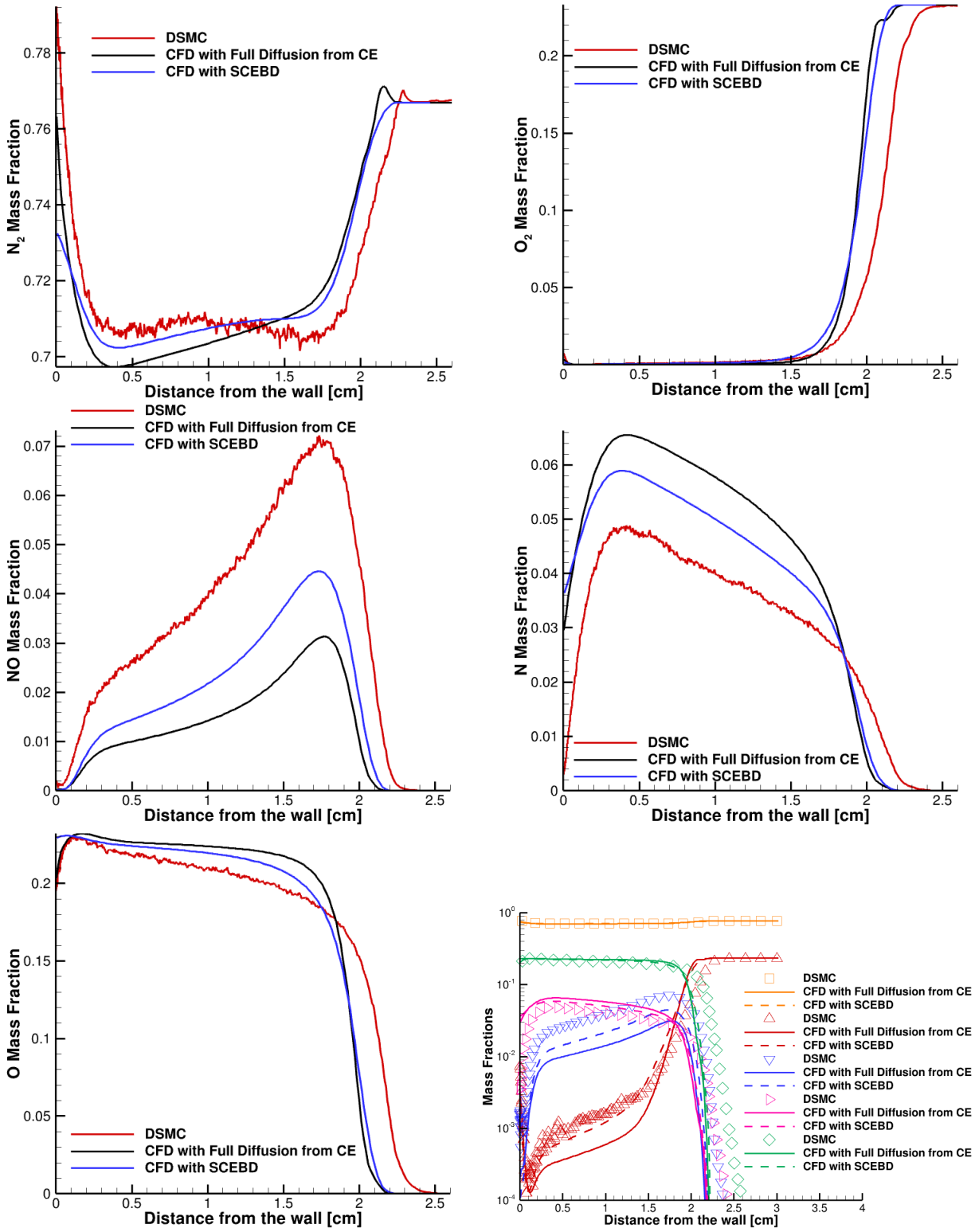

Figure 4.13: Mass fraction profiles comparison of MDGS and US3D solutions for the $5\,\mathrm{km\,s^{-1}}$ airflow around a cylinder case, extracted on the stagnation line and obtained with different diffusion models

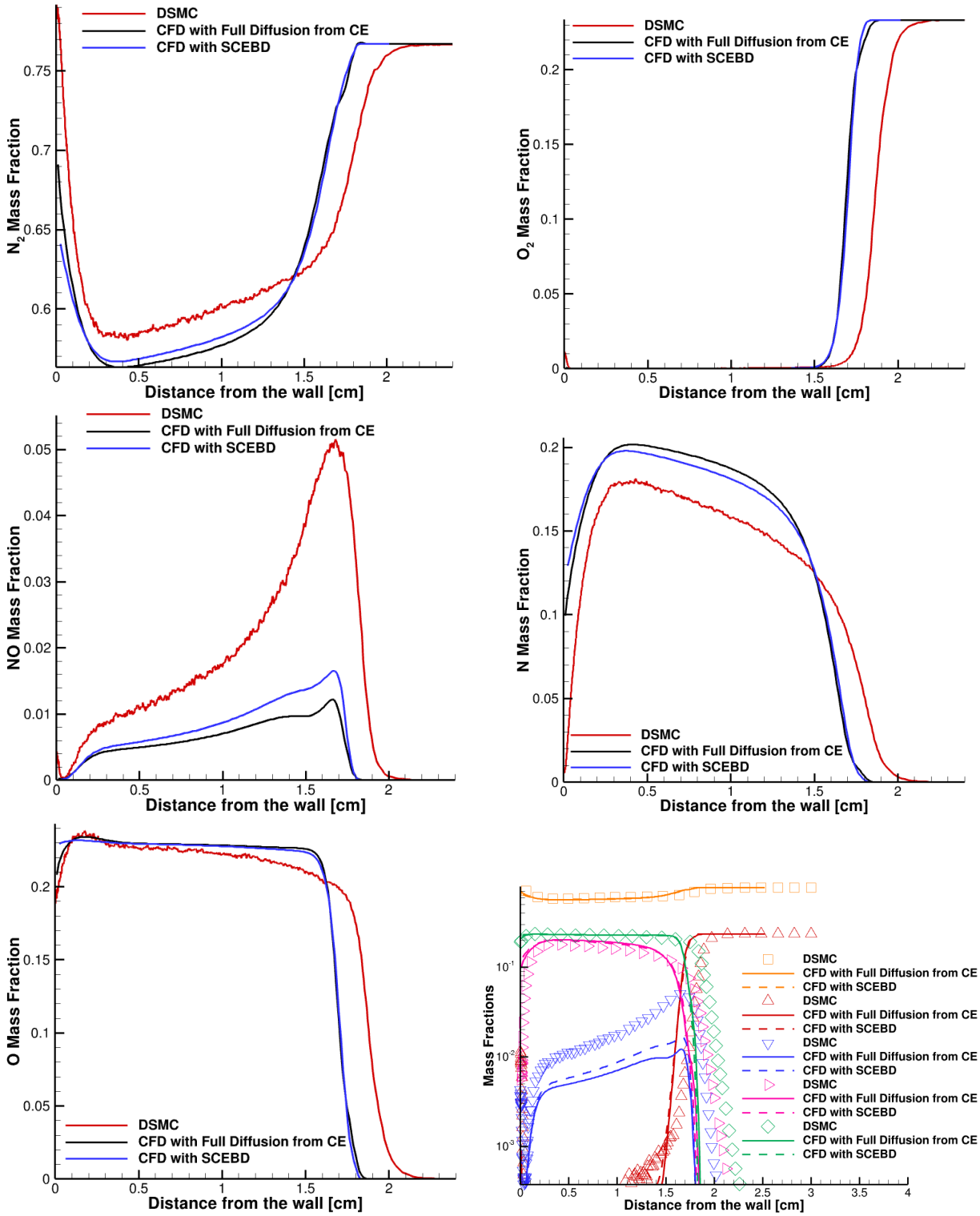

Figure 4.14: Mass fraction profiles comparison of MDGS and US3D solutions for the $6\,\mathrm{km\,s^{-1}}$ airflow around a cylinder case, extracted on the stagnation line and obtained with different diffusion models

Based on the results and the observed effects of the full diffusion, we want to quantify the contribution of the terms in Eq. 2.21 that are usually neglected. Thus, we define, for each species, the diffusion due to the mole fraction gradient as $D(X_s) = \nabla X_s$, the diffusion due to the temperature gradient as $D(T_s) = \chi_s \nabla(\ln T)$, and the diffusion due to the pressure gradient as $D(P_s) = (X_s - Y_s)\,\nabla(\ln P)$. Then, we estimate the importance of these terms relative to the full driving force d'_s from Eq. 2.21 and their distribution in the flow field in Figure 4.15.

$$\Delta_T(s) = \frac{|D(T_s)|}{|D(X_s)| + |D(T_s)| + |D(P_s)|} \qquad \Delta_P(s) = \frac{|D(P_s)|}{|D(X_s)| + |D(T_s)| + |D(P_s)|} \tag{4.1}$$

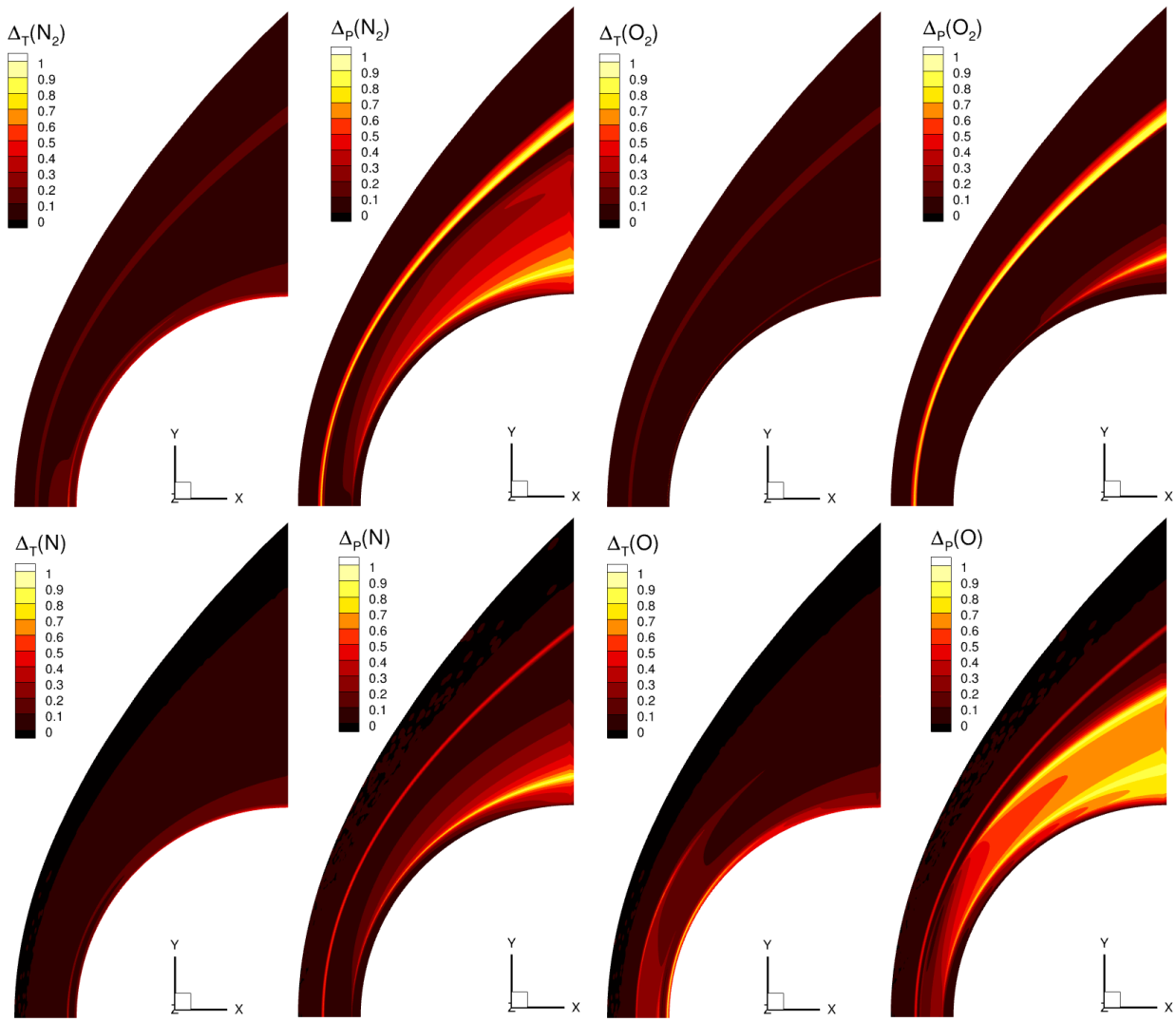

Figure 4.15: Comparison of the magnitude of diffusion terms due to the temperature and the pressure gradient to the full diffusion driving force for the cylinder at $4\,\mathrm{km\,s^{-1}}$.

The analysis shows that the diffusion due to the pressure gradient is the dominant contribution for both the molecular species in the shock region. The pressure gradient diffusion term shows dominant values in the post-shock region for the atomic species, $D(P_N)$ and $D(P_O)$. On the other hand, the wall area is taken over by the thermal diffusion term. The species N_2, N, and O are characterized by a thermal diffusion of comparable magnitude to the whole diffusion driving force. Additionally, the area close to the outflow in the $D(P_O)$ plot shows significant values of the pressure gradient term. However, because this region is characterized by very small gradients, the highlighted difference is numerical. These plots offer a qualitative analysis of the most affected areas, such as the wall and the shock.

4.2.2 Sphere and Sphere cone

Because the Soret, Dufour, and pressure terms have always been neglected in conventional CFD, this dissertation aims to investigate the dynamics of these phenomena and their features. Thus, we simulate the sphere test cases, described in Section 3.2.2.2, to investigate different geometry and wall conditions. In particular, as shown in the schematic diagram in Figure 3.7a, we set the wall to cold and isothermal and consider a range of catalytic efficiency γ from a non-catalytic to a full catalytic wall. First, We start with a non-catalytic wall boundary condition ($\gamma = 0$) and compare the solutions obtained by solving the different diffusion models, shown in Figure 4.16.

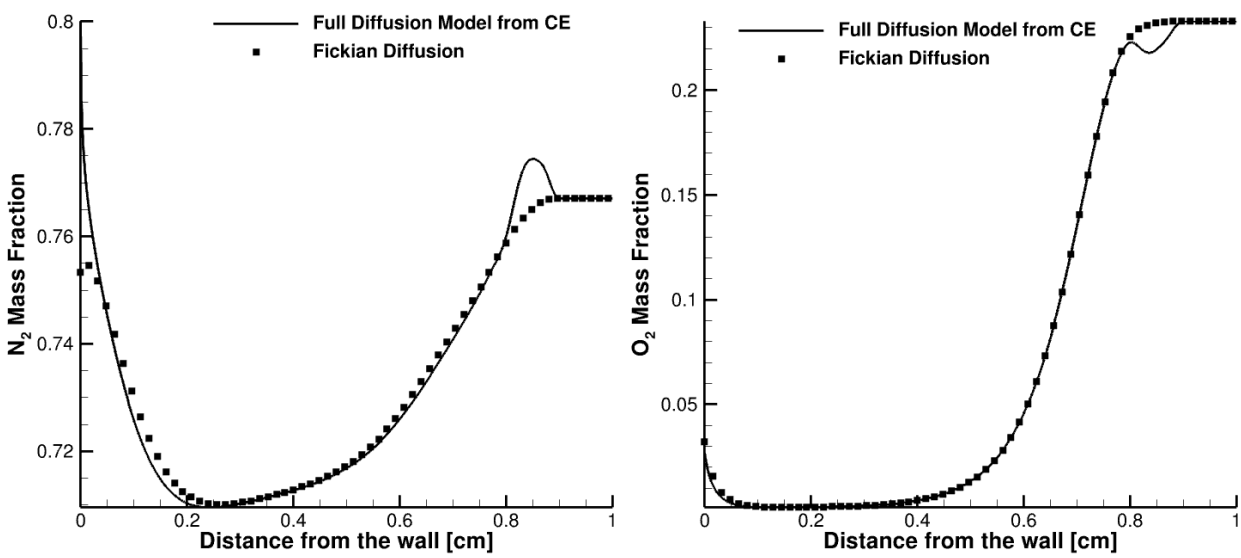

(a) N_2 mass fraction profile extracted at the stagnation line.

(b) O_2 mass fraction profile extracted at the stagnation line.

Figure 4.16: Comparison of the solutions obtained using the full diffusion model and considering only the Fickian contribution for the airflow around a sphere case.

As observed in the cylinder cases, the main differences appear in the mass fraction profiles of

the molecular species at the shock located around 9 mm from the wall. The full diffusion model captures a bump and a dent in the N_2 and the O_2 mass fraction profiles, respectively, that are not captured in the solution obtained without the thermal and the pressure diffusion. Furthermore, according to the full diffusion model solutions, the N_2 and O_2 mass fraction profiles have a higher wall value than the ones based solely on the Fickian contribution.

The trend captured at the shock is primarily due to the pressure gradient diffusion term, as shown in Figure 4.17. Whereas the thermal diffusion term is the primary contributor to the behavior observed at the wall. Specifically, the species N_2, N, and O are characterized by a thermal diffusion term of the same order of magnitude as the whole diffusion driving force.

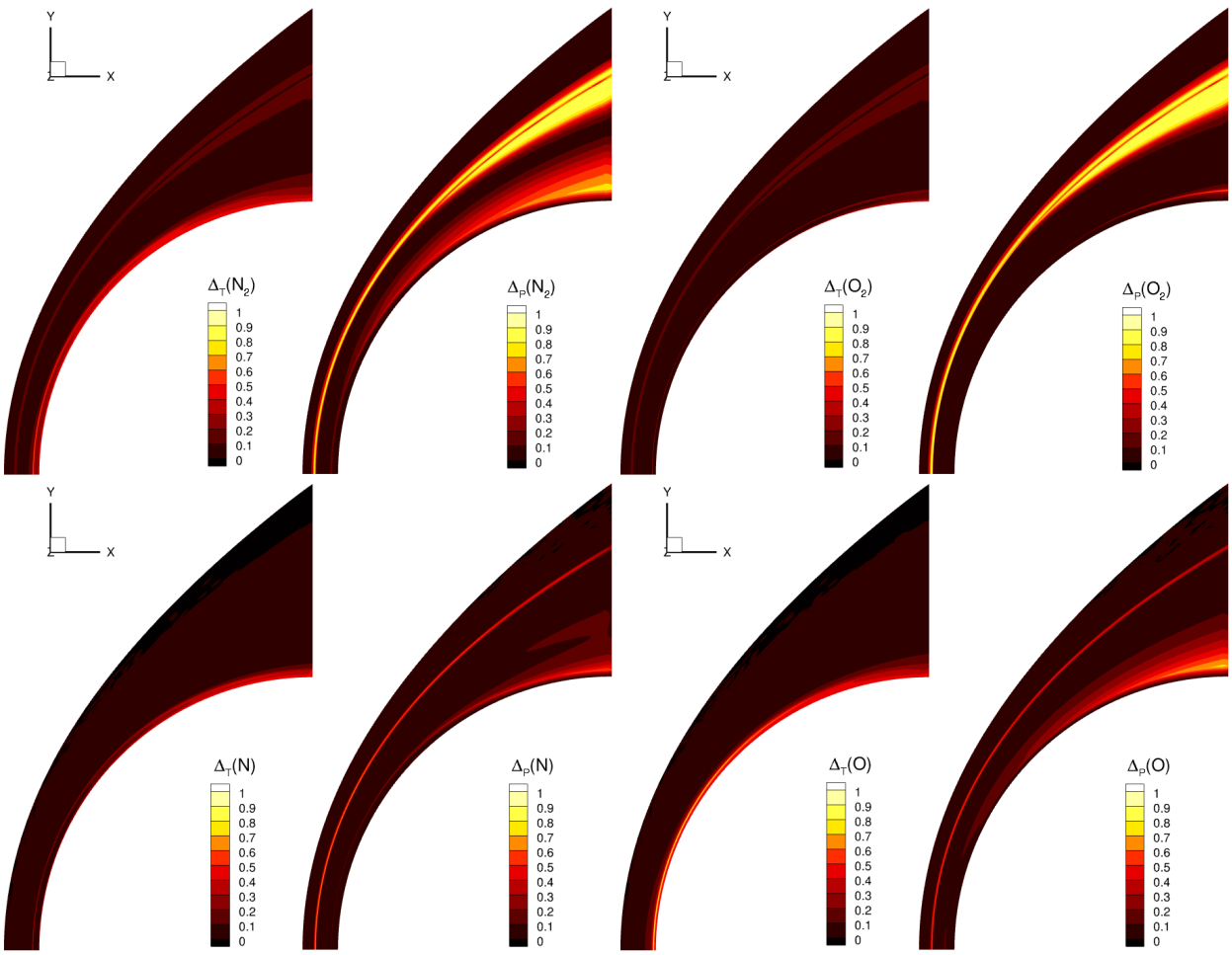

Figure 4.17: Magnitude comparison of the diffusion terms due to the temperature and the pressure gradient with the full diffusion driving force for the non-catalytic wall test case for the sphere case.

Figure 4.18 shows the comparison of the solutions in the near-wall region comparing the results at various catalytic efficiencies (γ). NO mass fraction is not included in the analysis because we

neglect the reactions involving the NO species in the catalytic boundary condition. By calculating the percentage difference between the solution obtained with the full diffusion model, q_{full}, and the one considering only the fickian contribution, q_{fickian}, as

$$\Delta_{\%} = \frac{|q_{\text{full}} - q_{\text{fickian}}|}{\left(\dfrac{q_{\text{full}} + q_{\text{fickian}}}{2}\right)},$$

we can see that $\Delta_{\%}$ decreases when we increase the catalytic efficiency γ.

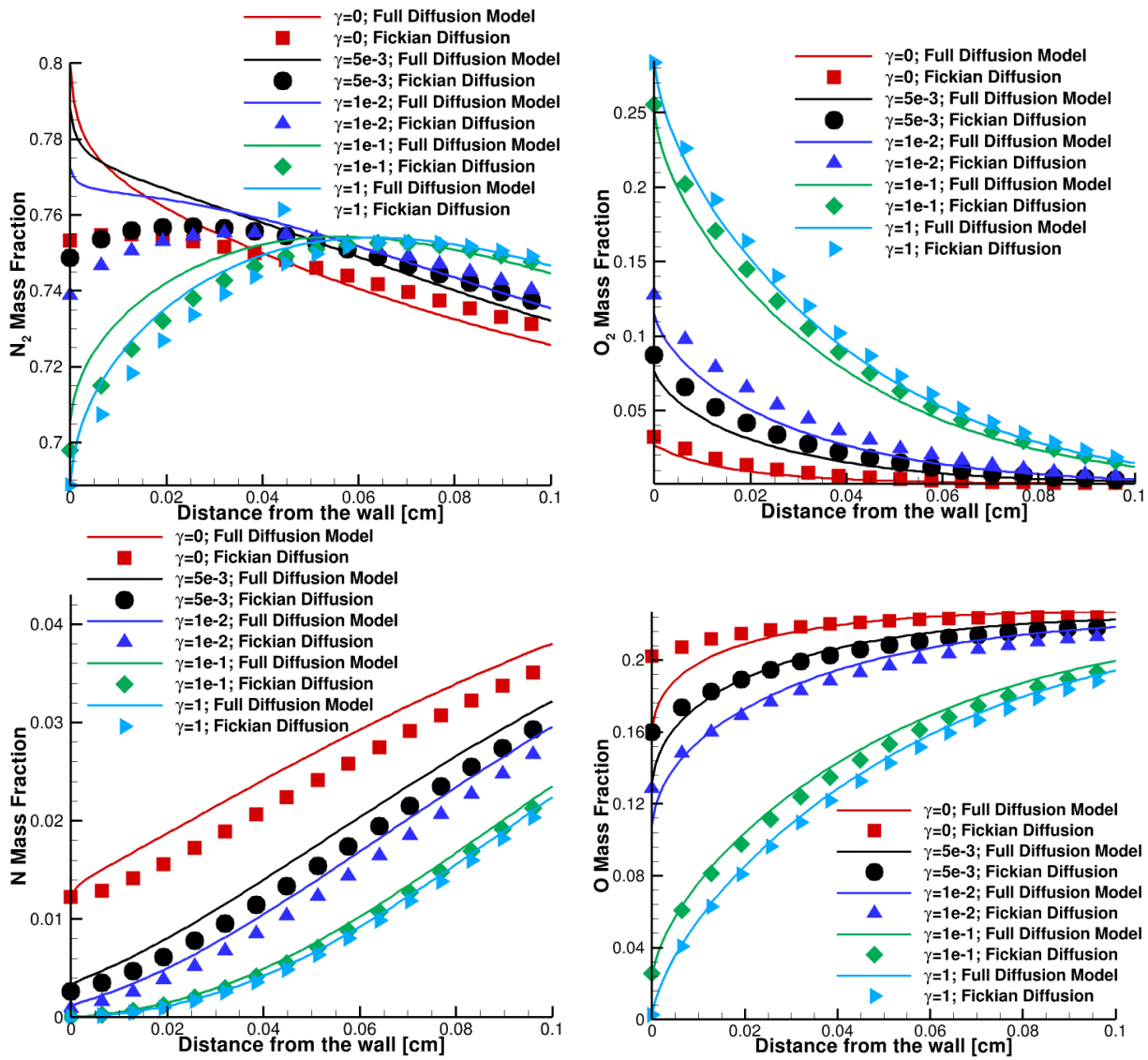

Figure 4.18: Comparison of the solutions obtained using different catalytic efficiencies zoomed for the airflow around a sphere case in the near-wall region.

Thus, the case with the non-catalytic boundary condition shows the most significant difference in the mass fraction profiles with a variation of 6% and 19.5% for the N_2 and the O_2 mass fraction profiles, respectively. On the other hand, for $\gamma = 1$, the difference is notably smaller, measuring at 0.015% and 0.31% for the N_2 and the O_2 mass fraction profiles. Figure 4.19 presents the heat flux profile on the sphere wall. Evaluating the percentage difference $\Delta_{\%}$ between the two diffusion models shows that the cases with small catalytic efficiencies γ are the most affected. Notably, as summarized on the y-axis of the plot on the left, the discrepancy between the solutions increases with the decrease of the catalytic efficiency. However, the trend is reversed for $\gamma = 10^{-2}$ and higher. This change can be attributed to the constraint enforced by the catalytic wall boundary condition. Since the flow is forced to react with the wall facilitating and its diffusive contribution considerably increases the heat flux at the surface, the Fickian diffusion contribution due to mass exchange becomes more dominant with the increase of the catalytic efficiency γ in the mass diffusion flux.

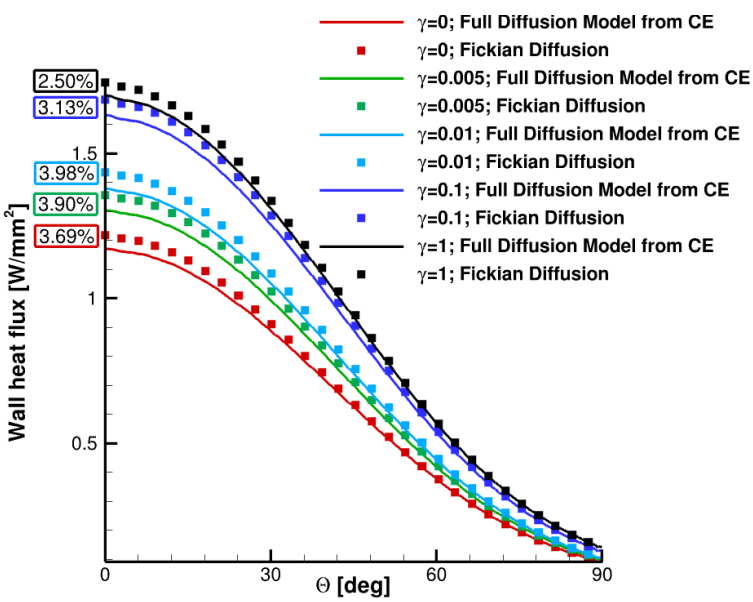

Figure 4.19: Comparison of the wall heat flux obtained using different catalytic efficiencies γ for the airflow around a sphere case.

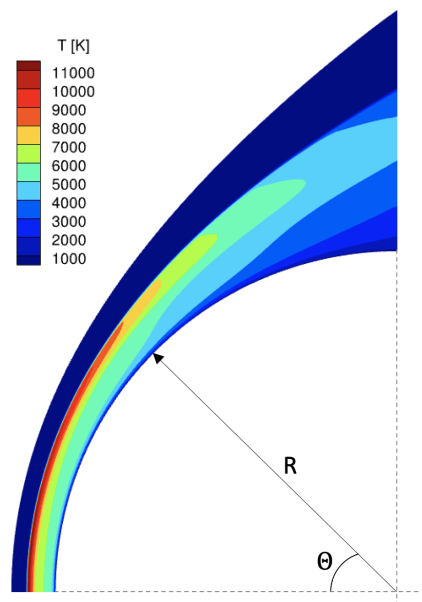

Figure 4.20: Temperature contour plot for the sphere case with $\gamma = 0$

4.2.3 Sphere-cone

After examining the solutions for the sphere, we explore how and if including the full diffusion model influences the flow at locations far from the nose by replicating the sphere test cases on a sphere cone geometry. Thus, as shown in Figure 3.8, we extract the data at the following locations: the stagnation line and 45° from it, before and after the entropy layer, and near the outflow. The comparison highlights that N_2 is the main species that show noticeable changes.

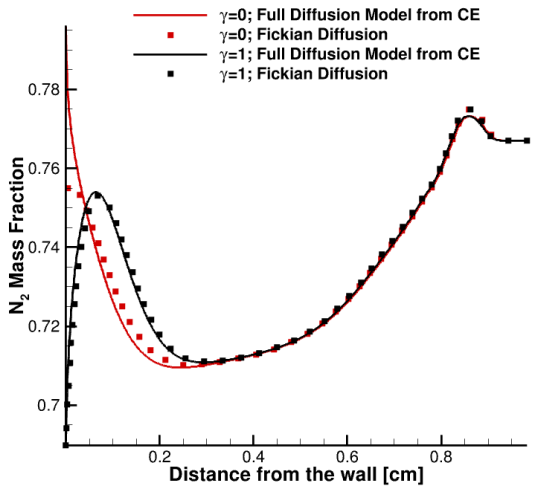

(a) Stagnation line

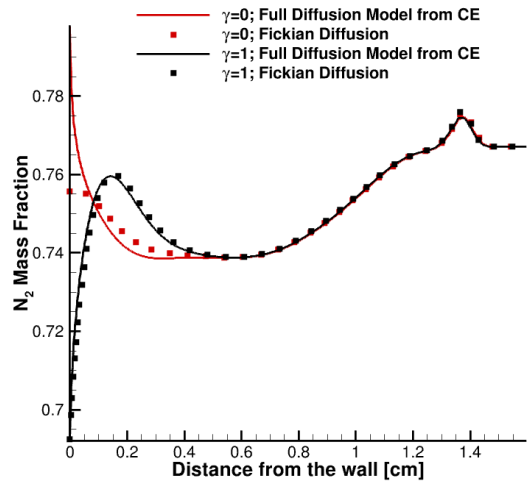

(b) 45° from the stagnation line

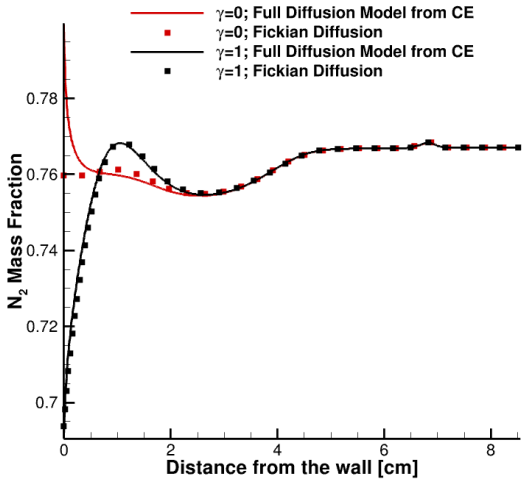

(c) Before the entropy layer

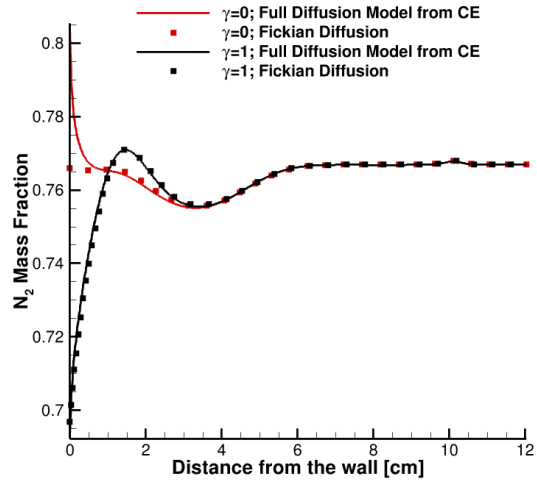

(d) After the entropy layer

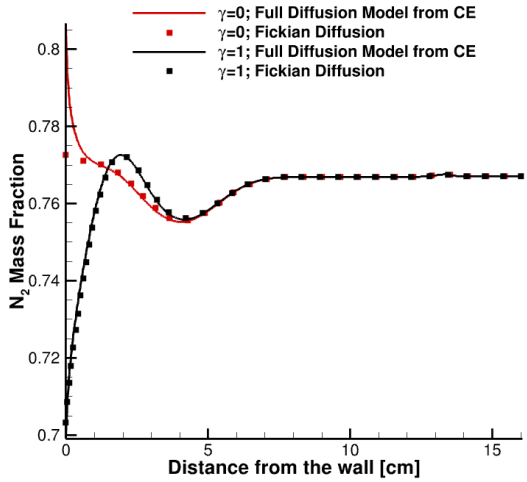

(e) Near-outflow

Figure 4.21: N_2 Mass fraction profiles at different locations for the sphere cone case.

As observed in the previous cases, the wall region is the most affected area because characterized by steep gradients. Figure 4.21 shows the N_2 mass fraction profile extracted at the locations mentioned above, and three main observations can be made. First, the case with the non-catalytic wall boundary condition undergoes the largest effects of the full diffusion model derived from the Chapman-Enskog theory. Second, we observe contrasting behaviors in the solutions at the extraction locations away from the nose. While the non-catalytic wall test case shows a decreasing difference between the solutions when moving along the body, we observe the opposite trend in the fully catalytic wall case. In the non-catalytic case, the discrepancy reaches 5.44% at the wall ($x = 0$) at the stagnation line escalating to 4.31% near the outflow. On the other hand, in the fully catalytic wall case, the difference is measured at 0.12% at the stagnation line, which then reduces to 0.59% near the outflow. The last observation is related to the solutions using the non-catalytic wall boundary conditions (gathered in Figures 4.21c-4.21e). The solution obtained by considering only the Fickian contribution to mass diffusion presents a plateau in the N_2 mass fraction. However, when the full diffusion model is used, the N_2 mass fraction experiences a gradual increase at the wall, reaching a value greater than the free-stream condition.

Figure 4.22 is obtained by calculating the magnitude of the thermal and pressure diffusion using Equation 4.1, as done before with the sphere case. Figure 4.22 shows the contour plot of Δ_T and Δ_P for the molecular species N_2 and O_2 and for the atomic species N and O. We can observe that the dominant contribution to the molecular species diffusion in the shock region is the term dependent on the pressure gradient. When we move downstream, in the region near the outflow, the thermal diffusion presents comparable magnitude, but it is overpowered by the term dependent on the pressure gradient. The contour plots for the atomic species show that the near-wall region is primarily influenced by the temperature term. This behavior is reflected in the discrepancy observed in Figure 4.21. The pressure term becomes noticeable around the nose in both the shock and the near-wall region. This trend is expected being those regions characterized by steep pressure gradients.

4.3 Concluding Remarks

Chapter 4 gathers the results of the problems described in Chapter 3, which are used to study the transport and diffusive effects in hypersonic flows. The results have shown the importance of comparing the solutions obtained using DSMC and CFD codes with consistent models. In particular, by analyzing the CFD solutions obtained with the full diffusion model from CET, we observed the effects of the Soret, pressure, and Dufour terms on the flow field. For the chosen test cases, these additional terms can not be neglected because they play an important role in areas such as the shock and the wall region. The conclusions that these results helped us draw are summarized in the next chapter.

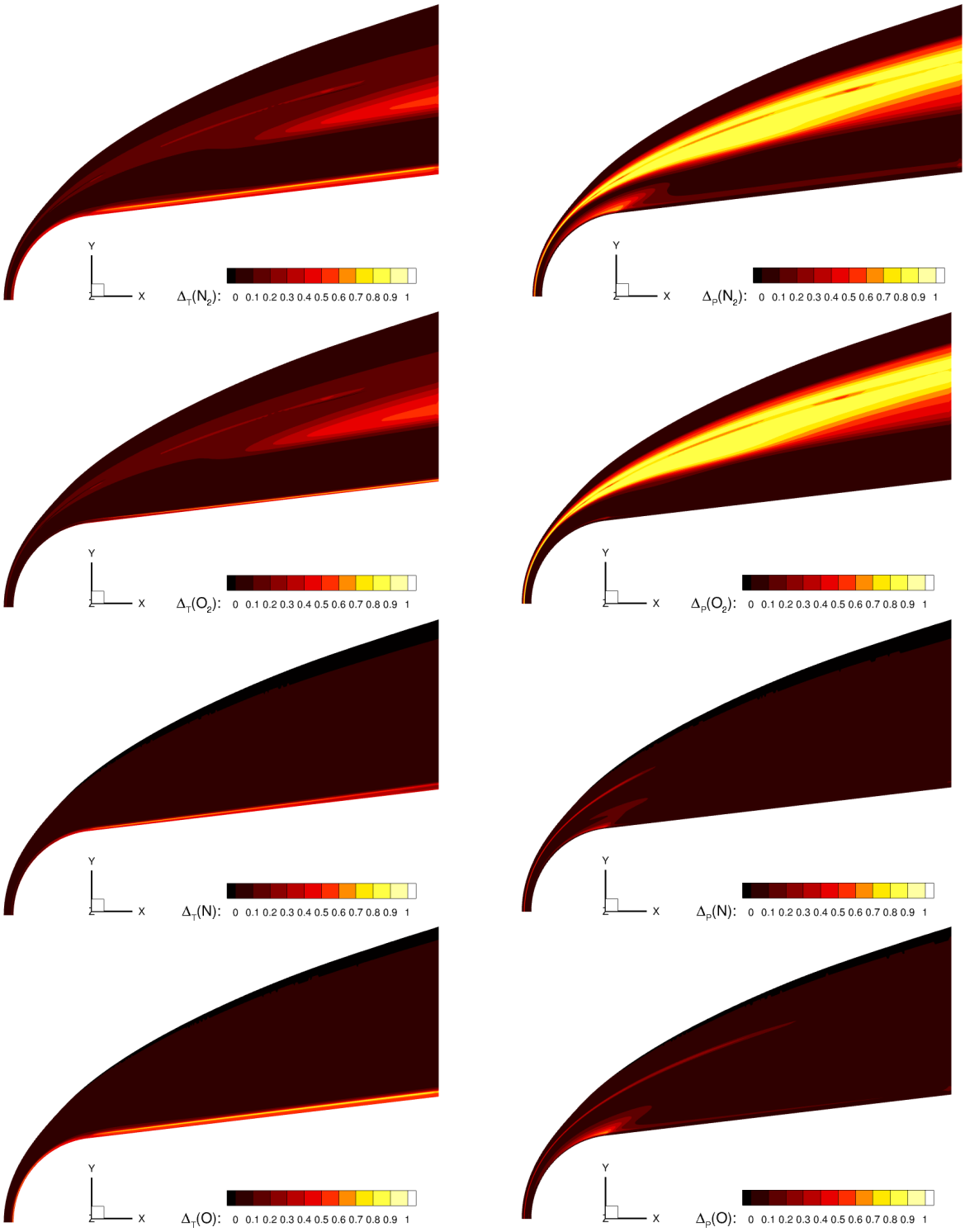

Figure 4.22: Magnitude comparison of diffusion terms due to the temperature and the pressure gradient with respect to the full diffusion driving force of N_2, O_2, N, and O for the non-catalytic wall test case.

Chapter 5

Conclusions

Chapter 5 provides the conclusions from which we can extract by observing and analyzing the results shown in the previous chapter. In addition, we conclude the chapter by offering some research perspectives on future work.

5.1 Contributions of this Work

This dissertation aims to study hypersonic flows in the near continuum regime, focusing on diffusion and transport processes. From the first to the last chapter, we analyze the characteristics of hypersonic flows, how we can model them, and the main tools available in the literature.

This work started with a validation study conducted primarily on simple one-dimensional problems using a monatomic gas mixture. The solutions showed that US3D and MGDS agree very well when the models are consistent. Hence, the results allowed us to solve more complex geometries and mixtures. Starting with a two-dimensional shear flow and a monatomic Argon gas, we compared the CFD and the DSMC solutions far from the inflow discontinuity. As expected, the US3D transport models provided similar results to the VHS model. Now that we implemented the VHS-based transport properties for monatomic gas in the CFD code and verified to be in agreement with the DSMC results, we further investigate the transport phenomena by including another level of complexity: the transport of mass in a gas mixture.

Thus, we solve hypersonic flows over a cylinder of a 10 cm radius in the near-continuum regime, setting the Knudsen number equal to $Kn = 0.001$ and a five-species air mixture at three free stream velocities. First, we investigate the effects of the different chemical kinetics models to assess the effect of the model inconsistency between CFD and DSMC, since we accepted such limitation. As expected, the differences in the solutions between the CFD solutions using the Park and MMT models and the DSMC with the TCE chemistry model can be analyzed to understand the underlying differences between the kinetic models. The differences between the CFD solutions are the most significant for the lowest enthalpy test case ($4\,\mathrm{km\,s^{-1}}$ flow), where only partial Oxygen dissociation

takes place. The model predictions converge as the enthalpy increases ($6\,\mathrm{km\,s^{-1}}$ flow) where the Oxygen dissociates entirely.

An intriguing observation arises from comparing the CFD and DSMC solutions. The mass fractions of species near the wall differ noticeably. In particular, the DSMC solutions consistently present a depletion of atomic species followed by an accumulation of molecular species in the near-wall region for each condition examined. While these differences were expected because of the inconsistency in the chemical kinetics models, the behavior of the species at the wall emphasized the need for further investigation and the understanding of the responsible mechanisms of such behavior. Upon examination, it was determined that the observed discrepancy was attributed to the diffusion effects. We repeated the simulations utilizing the Mutation++ open-source library within the US3D framework to further explore this phenomenon. In these simulations, the transport coefficients were calculated using the Stefan-Maxwell equations. Surprisingly, the results obtained using the Stefan-Maxwell equations exhibited differences of only around 3% compared to the solutions employing the SCEBD model for the transport coefficients. However, having analyzed the Stefan-Maxwell equations and the Chapman-Enskog approximation, we know that none of the CFD simulations considered in this study included the thermal and pressure diffusion terms, as they are commonly neglected in most CFD codes.

By analyzing the magnitude of the thermal-diffusion term, we discovered that, under the studied conditions, this term should dominate the species' diffusion near the wall due to the presence of a significant temperature gradient. Thus, we implemented, in the CFD solver, the full diffusion model derived from the Chapman-Enskog theory focusing on studying the additional terms in the diffusion driving force and heat flux, usually neglected when simulating hypersonic flows with CFD solvers. We replicated the cylinder test cases using the full diffusion model from the Chapman-Enskog theory approximation to quantify the effects of the diffusion model. Our observations revealed that the areas most significantly impacted by the full diffusion model derived from CET are the shock location and the near-wall region. In particular, the solutions showed that what we considered noise scatter at the shock location in the DSMC simulation is physical and is captured by the CFD solutions obtained with the full diffusion model. Despite the lack of complete agreement between the solutions, primarily due to differences in the chemistry models employed, it is noteworthy that the CFD solution with the full diffusion model successfully reproduces the trends observed in the DSMC solutions. In other words, while there may be quantitative differences, the CFD solution fully replicates the qualitative behavior and trends with the full diffusion model.

The dissertation continues by comparing the solutions obtained with CFD using the available transport models and the approximation derived from CET to evaluate the necessity of solving the full transport system in CFD in the near-continuum regime. We chose test cases using different geometries and sets of initial and boundary conditions. In particular, we selected a sphere and a sphere-cone of 10 cm nose-radius because of their relevance to hypersonic research. For these

geometries, we set the density so that the flow is in the near continuum regime, the free-stream velocity to be $4\,\mathrm{km\,s^{-1}}$ and a hot slip wall boundary conditions with different catalytic efficiencies.

In the sphere case results, the molecular species N_2 and O_2 showed distinct features in their mass fraction profiles at the shock location. When we included the diffusion terms dependent on temperature and pressure gradients in the CFD solver, we observed a bump in the mass fraction profile of N_2 and a dent in the mass fraction profile of O_2 at the stagnation line. The pressure term emerged as the dominant factor contributing to these effects, due mainly to the flow compression across the shock. Moreover, the effects of the full diffusion model on the near-wall region are the most relevant when the wall is set to be non-catalytic, with $\gamma = 0$. Then, the differences with the fickian diffusion model diminished with the increase of the catalytic efficiency. This trend was expected since the lowest catalytic efficiency values γ were considered extreme conditions because the wall is considered fully or almost entirely indifferent to kinetics. By increasing the catalytic efficiency, we introduced a constraint at the wall, enhancing reactions and/or recombination in that region and, subsequently, influencing the diffusive processes that adhere to the boundary conditions. As a result, the Fickian contribution becomes the dominant factor in the mass diffusion with the increase of the catalytic efficiency because of the steeper concentration gradients.

Similar observations can be made by observing the sphere-cone case solutions, specifically in the near-wall region and away from the nose area. In particular, the species N_2 showed the most significant effects of the full diffusion model, displaying a contrasting trend compared to the solution obtained by neglecting the temperature and pressure terms in the diffusion driving force.

5.2 Future work

Because of the significant effects of the chemical kinetics model on the solutions shown in section 4, further comparisons are necessary to fully understand the importance of implementing the full diffusion model when solving hypersonic flows and further analyze the different contributions.

Thus, we will conduct a study on the cylinder case involving the non-reacting binary mixture. The presence of a non-reacting flow will allow us to perform meaningful comparisons without the issue of inconsistent chemical models and isolate the effects of the diffusion models. We choose Argon and Helium as species and a set of initial and boundary conditions that allow us to replicate realistic post-shock conditions, as explained in Section 3.2.2.1.

Figures 5.1 present the preliminary CFD results for the case at the highest free-stream velocity. Figures 5.2 is the zoom of Figures 5.1 at the shock location on the top and the near-wall region on the bottom. These figures represent the comparison of the species mass fraction profiles, extracted at the stagnation line, for a flow characterized by a free-stream velocity of $8\,\mathrm{km\,s^{-1}}$ using different diffusion models. Furthermore, we compare the solutions obtained with different free-stream densities. The case with $\rho = 3.74 \times 10^{-4}$ is the case in the near-continuum regime. Then, we

simulate a more continuum and rarefied flow by increasing and decreasing the free-stream density. As expected, when the only contribution to diffusion is the fickian term, the gas concentration stays constant since no reactions will trigger changes in the composition. However, as Figures 5.1 show, when the full diffusion model is taken into account, striking behaviors appear in the regions with the steepest gradients, the shock, and the wall.

When the full diffusion model is taken into account, striking behaviors appear in the regions with the steepest gradients, the shock, and the wall. As expected, with the increase in density, the shock gets closer to the wall, and its width decreases. Moreover, the effects of including the full diffusion model derived from CET become more evident as the density decreases. This trend is validated by the fact that the closer we get to the rarefied regime, the stronger the translational non-equilibrium phenomena are.

These plots are the preliminary analysis aiming to find an envelope of conditions where these effects are highly relevant. Then, based on the CFD solutions, the DSMC simulations will be set, run, and used as a reference in the comparison in the near future. The comparison will allow us to analyze in detail the unique features captured by the CFD using the full diffusion model from CET. Finally, future work will address the difference in the chemical kinetics models between the CFD and the DSMC solvers.

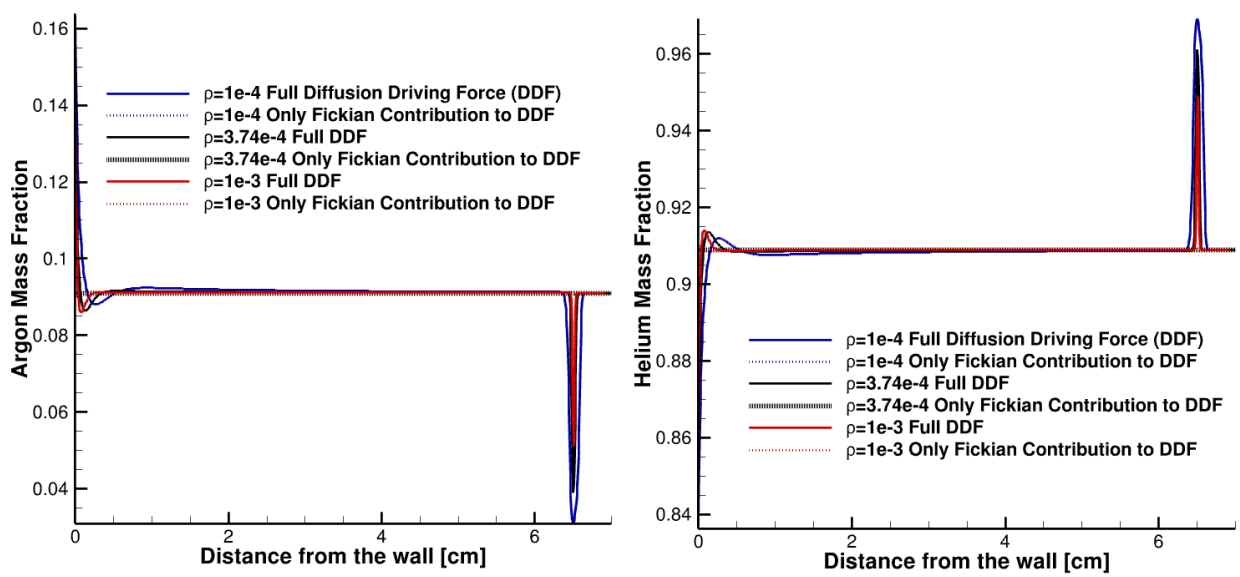

Figure 5.1: Comparison of the species mass fraction for the 8 km/s binary flow around a cylinder case on the stagnation line obtained using different diffusion models

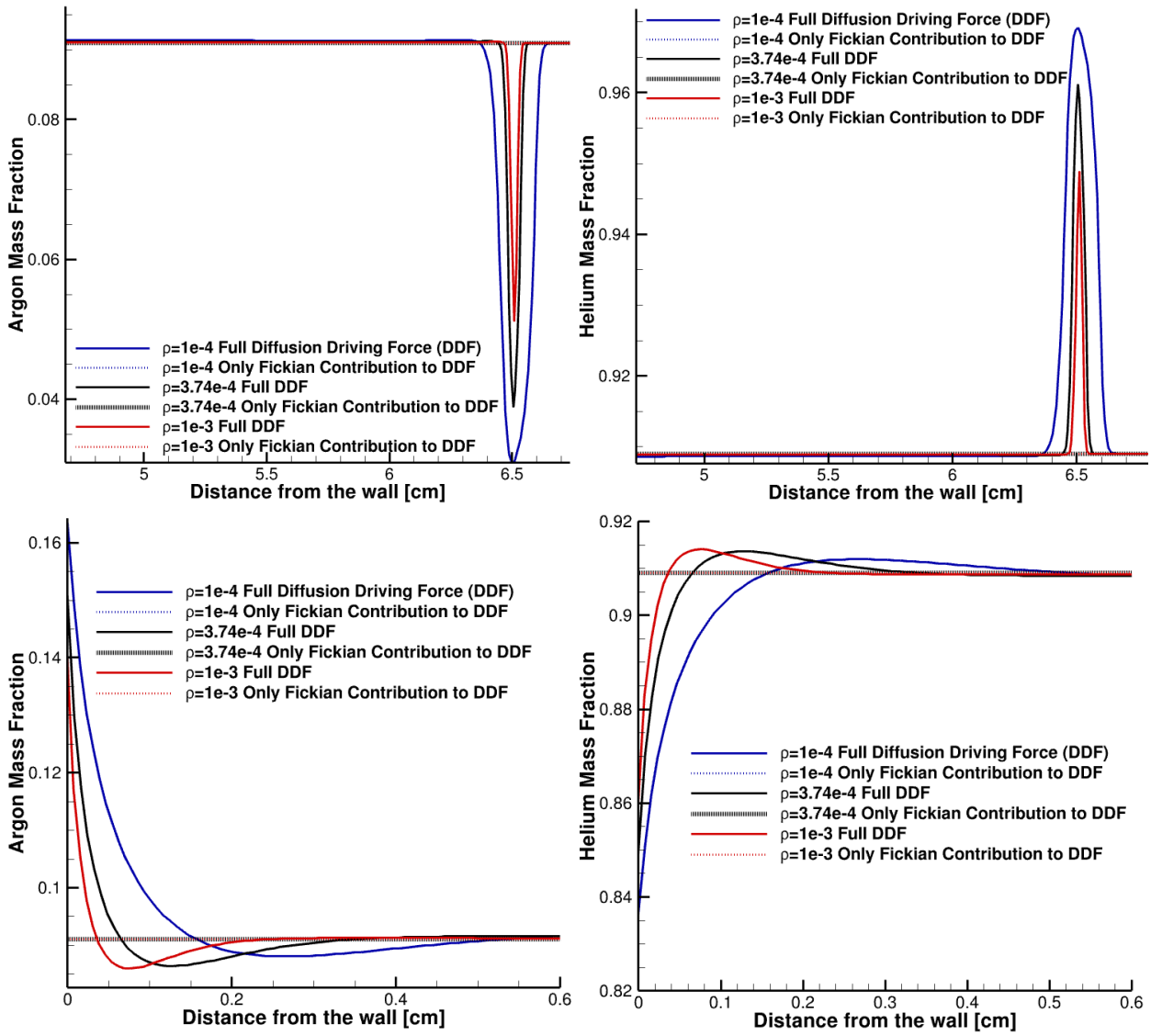

Figure 5.2: Zoom in the shock (on the top) and wall (on the bottom) areas for the 8 km/s binary flow around a cylinder case on the stagnation line obtained using different diffusion models

Bibliography

[1] Thomas Edward Schwartzentruber. *A modular particle-continuum numerical algorithm for hypersonic non-equilibrium flows*. PhD thesis, Citeseer, 2007.

[2] John D Ramshaw and CH Chang. Friction-weighted self-consistent effective binary diffusion approximation, 1996.

[3] John D Ramshaw. Hydrodynamic theory of multicomponent diffusion and thermal diffusion in multitemperature gas mixtures. 1993.

[4] Roop N Gupta, Jerrold M Yos, Richard A Thompson, and Kam-Pui Lee. A review of reaction rates and thermodynamic and transport properties for an 11-species air model for chemical and thermal nonequilibrium calculations to 30000 k. *NASA Reference Publication*, (1232), 1990.

[5] CR Wilke. A viscosity equation for gas mixtures. *The journal of chemical physics*, 18(4): 517–519, 1950.

[6] Frederick Gwynn Blottner, Margaret Johnson, and Molly Ellis. Chemically reacting viscous flow program for multi-component gas mixtures. Technical report, Sandia Labs., Albuquerque, N. Mex., 1971.

[7] William Sutherland. Lii. the viscosity of gases and molecular force. *The London, Edinburgh, and Dublin Philosophical Magazine and Journal of Science*, 36(223):507–531, 1893.

[8] Ross S Chaudhry and Graham V Candler. Statistical analyses of quasiclassical trajectory data for air dissociation. In *AIAA Scitech 2019 Forum*, page 0789, 2019.

[9] Ross Chaudhry. Modeling and analysis of chemical kinetics for hypersonic flows in air. 2018.

[10] Ross S Chaudhry, Iain D Boyd, Erik Torres, Thomas E Schwartzentruber, and Graham V Candler. Implementation of a chemical kinetics model for hypersonic flows in air for high-performance cfd. In *AIAA Scitech 2020 Forum*, page 2191, 2020.

[11] Jason D Bender, Paolo Valentini, Ioannis Nompelis, Yuliya Paukku, Zoltan Varga, Donald G Truhlar, Thomas Schwartzentruber, and Graham V Candler. An improved potential energy surface and multi-temperature quasiclassical trajectory calculations of n2+ n2 dissociation reactions. *The Journal of chemical physics*, 143(5):054304, 2015.

[12] Yuliya Paukku, Ke R Yang, Zoltan Varga, and Donald G Truhlar. Global ab initio ground-state potential energy surface of n4. *The Journal of chemical physics*, 139(4):044309, 2013.

[13] Zoltan Varga, Yuliya Paukku, and Donald G Truhlar. Potential energy surfaces for o+ o2 collisions. *The Journal of chemical physics*, 147(15):154312, 2017.

[14] Evgeniĭ Evgenevich Nikitin. Theory of elementary atomic and molecular processes in gases(book). *Oxford, Clarendon Press*, 1974.

[15] Graeme A Bird. Molecular gas dynamics and the direct simulation of gas flows. *Molecular gas dynamics and the direct simulation of gas flows*, 1994.

[16] Graeme A Bird and JM Brady. *Molecular gas dynamics and the direct simulation of gas flows*, volume 5. Clarendon press Oxford, 1994.

[17] Wolfgang Wagner. A convergence proof for bird's direct simulation monte carlo method for the boltzmann equation. *Journal of Statistical Physics*, 66(3-4):1011–1044, 1992.

[18] SYDNEY CHAPMAN and TG Cowling. Non-uniform gases. *Cambridge Univ. Press, Cambridge, 1952; Inostrannaya Literatura, Moscow, 1960*, 1952.

[19] Erik Torres, Georgios Bellas-Chatzigeorgis, and Thierry E Magin. How to build coarse-grain transport models consistent from the kinetic to fluid regimes. *Physics of Fluids*, 33(3):036110, 2021.

[20] Thierry E Magin and Gérard Degrez. Transport algorithms for partially ionized and unmagnetized plasmas. *Journal of computational Physics*, 198(2):424–449, 2004.

[21] Iain D. Boyd and Thomas E. Schwartzentruber. *Nonequilibrium Gas Dynamics and Molecular Simulation*. Cambridge University Press, 2017.

[22] DJ Rader, MA Gallis, JR Torczynski, and W Wagner. Direct simulation monte carlo convergence behavior of the hard-sphere-gas thermal conductivity for fourier heat flow. *Physics of Fluids*, 18(7):077102, 2006.

[23] Thomas E Schwartzentruber and Iain D Boyd. A hybrid particle-continuum method applied to shock waves. *Journal of Computational Physics*, 215(2):402–416, 2006.

[24] Thomas E Schwartzentruber, Leonardo C Scalabrin, and Iain D Boyd. Hybrid particle-continuum simulations of nonequilibrium hypersonic blunt-body flowfields. *Journal of Thermophysics and Heat Transfer*, 22(1):29–37, 2008.

[25] T.E. Schwartzentruber, L.C. Scalabrin, and I.D. Boyd. A modular particle–continuum numerical method for hypersonic non-equilibrium gas flows. *Journal of Computational Physics*, 225 (1):1159 – 1174, 2007.

[26] Kelly Stephani, D Goldstein, and P Varghese. Development of a hybrid dsmc/navier-stokes solver with application to the sts-119 boundary layer transition flight experiments. In *49th AIAA Aerospace Sciences Meeting including the New Horizons Forum and Aerospace Exposition*, page 534, 2011.

[27] KA Stephani, David B Goldstein, and Philip L Varghese. Consistent treatment of transport properties for five-species air direct simulation monte carlo/navier-stokes applications. *Physics of fluids*, 24(7):077101, 2012.

[28] KA Stephani, David B Goldstein, and Philip L Varghese. A non-equilibrium surface reservoir approach for hybrid dsmc/navier–stokes particle generation. *Journal of Computational Physics*, 232(1):468–481, 2013.

[29] James B Scoggins and Thierry E Magin. Development of mutation++: Multicomponent thermodynamic and transport properties for ionized plasmas written in c++. In *11th AIAA/ASME joint thermophysics and heat transfer conference*, page 2966, 2014.

[30] Timothy D. Holman and Iain D. Boyd. Effects of continuum breakdown on hypersonic aerothermodynamics for reacting flow. *Physics of Fluids*, 23(2):027101, 2011.

[31] Michael J Wright, Graham V Candler, and Deepak Bose. Data-parallel line relaxation method for the navier-stokes equations. *AIAA journal*, 36(9):1603–1609, 1998.

[32] Graham V Candler, Heath B Johnson, Ioannis Nompelis, Vladimyr M Gidzak, Pramod K Subbareddy, and Michael Barnhardt. Development of the us3d code for advanced compressible and reacting flow simulations. In *53rd AIAA Aerospace Sciences Meeting*, page 1893, 2015.

[33] Ross Taylor and Rajamani Krishna. *Multicomponent mass transfer*, volume 2. John Wiley & Sons, 1993.

Appendix A

Transport models parameters

Table A.1: Blottner viscosity model coefficients.

Species	A_s	B_s	C_s
N_2	0.0268142	0.3177838	-11.3155513
O_2	0.0449290	-0.0826158	-9.2019475
NO	0.0436378	-0.0335511	-9.5767430
N	0.0115572	0.6031679	-12.4327495
O	0.0203144	0.4294404	-11.6031403

Table A.2: VHS parameters

Species	d_{ref}	ω
Ar	3.92d-10	0.31d0
He	2.33d-10	0.16d0
N_2	4.17d-10	0.24d0
O_2	4.07d-10	0.27d0
NO	4.20d-10	0.29d0
N	3.00d-10	0.30d0
O	3.00d-10	0.30d0

Appendix B

Chapman-Enskog Parameters

This appendix summarizes the transport matrices and coefficients derived from CET.

$$G^D_{sp} = G^D_{ps} = -\frac{X_s X_p}{\mathcal{D}_{sp}} \qquad s,p \in S \text{ and } s \neq p$$

$$G^D_{ss} = \sum_{\substack{p\in S\\ p\neq s}} \frac{X_s X_p}{\mathcal{D}_{sp}} \qquad s \in S$$

$$\mathcal{D}_{sp} = \frac{3}{16nQ^{(1,1)}_{sp}}\sqrt{\frac{2\pi k_B T\left(m_p+m_s\right)}{m_s m_p}} \qquad s,p \in S \text{ and } s \neq p$$

$$G^\mu_{sp} = G^\mu_{ps} = X_s X_p \frac{16}{5}\sqrt{\frac{2m_s m_p}{\pi k_B T\left(m_p+m_s\right)^3}}\left(Q^{(2,2)}_{sp} - \frac{5}{3}Q^{(1,1)}_{sp}\right) \qquad s,p \in S \text{ and } s \neq p$$

$$G^\mu_{ss} = \sum_{\substack{p\in S\\ p\neq s}} X_s X_p \frac{16}{5}\sqrt{\frac{2m_s m_p}{\pi k_B T\left(m_p+m_s\right)^3}}\left(Q^{(2,2)}_{sp}\frac{m_p}{m_s} - \frac{5}{3}Q^{(1,1)}_{sp}\right) + \frac{X_s^2}{\eta_s} \qquad s,p \in S$$

$$G^\kappa_{sp} = G^\kappa_{ps} = \frac{1}{25k_B}\frac{X_s X_p}{n\mathcal{D}_{sp}}\frac{m_s m_p}{\left(m_p+m_s\right)^2}\left(16A^*_{sp} + 12B^*_{sp} - 55\right) \qquad s,p \in S \text{ and } s \neq p$$

$$G^\kappa_{ss} = \frac{1}{25k_B}\sum_{\substack{p\in S\\ p\neq s}} \frac{X_s X_p}{n\mathcal{D}_{sp}}\frac{\left(30m_s^2 + 25m_p^2 - 12m_p^2 B^*_{sp} + 16m_s m_p A^*_{sp}\right)}{\left(m_p+m_s\right)^2} + \frac{4}{15k_B}\frac{X_s^2 m_s}{\eta_s} \qquad s,p \in S$$

$$\Lambda^{01}_{sp} = \Lambda^{01}_{ps} = \frac{1}{25k_B}\frac{X_s X_p}{n\mathcal{D}_{sp}}\frac{m_s}{\left(m_p+m_s\right)}\left(12C^*_{sp} - 10\right) \qquad s,p \in S \text{ and } s \neq p$$

$$\Lambda^{01}_{ss} = -\frac{1}{25k_B}\sum_{\substack{p\in S\\ p\neq s}} \frac{X_s X_p}{n\mathcal{D}_{sp}}\frac{m_p}{\left(m_p+m_s\right)}\left(12C^*_{sp} - 10\right) \qquad s,p \in S$$

$$A^*_{sp} = \frac{Q^{(2,2)}_{sp}}{Q^{(1,1)}_{sp}} \qquad s, p \in S$$

$$B^*_{sp} = \frac{5Q^{(1,2)}_{sp} - 4Q^{(1,3)}_{sp}}{Q^{(1,1)}_{sp}} \qquad s, p \in S$$

$$C^*_{sp} = \frac{Q^{(1,2)}_{sp}}{Q^{(1,1)}_{sp}} \qquad s, p \in S$$

$$\eta^*_{sp} = \frac{5}{16}\frac{\sqrt{\pi k_B T m_s}}{Q^{(2,2)}_{ss}} \qquad s \in S$$

Appendix C

Implementation in US3D

The test cases have been solved using a standard finite-volume approach. In particular, Equations 2.1, 2.2 and 2.3 can be written in the conservative form:

$$\frac{\partial U}{\partial t} + \nabla_x F = W \tag{C.1}$$

where U is the state variable vector, defined as $U = [\rho_s, \rho\mathbf{v}, \rho E]^T$, F is the total flux vector, composed of a convective and a diffusive component, and W is the source term vector. In the finite volume formulation, the weak form of Equation C.1 is obtained by integrating over an arbitrary fixed control volume Ω. The time integration is performed with an implicit DPLR method [31]. A second-order MUSCL scheme with a pressure limiter is used to limit overshoots in regions of strong shocks. The convective fluxes are computed using the modified Steger-Warming flux vector splitting method for steady-state simulations. [32]

While canonical spatial and temporal integration methods have been used to develop this study, implementing the transport model derived from CET requires some caution to accommodate the addition of the new transport terms. In particular, the Stefan-Maxwell matrix G^D_{sp} is singular due to the constraint imposed on the species mass fluxes, shown in Eq. 2.4. Moreover, when the viscous flux is expressed using the CET and linearized, the Jacobian presents non-zero entries that must be included in the numerical modeling. The following paragraphs address both these problems.

C.1 Diffusion Transport Matrix Singularity due to Mass Conservation Constraint

Due to the mass constraint expressed in Eq. 2.20, the SM system is singular. However, we can write Eq. 2.20 in terms of the mass diffusion flux $\mathbf{j}^D_s$, as shown in Eq. C.2, and solve for the $(n_s - 1)$ independent equations [33]

$$\mathbf{d}^D_s = -\sum_{\substack{p=1 \\ p\neq s}}^{n_s} \frac{X_s\,\mathbf{j}^D_p - X_p\,\mathbf{j}^D_s}{c_t\,\mathscr{D}_{sp}} \qquad \text{where} \quad c_t = \frac{\rho}{M_{mix}}. \tag{C.2}$$

In particular, knowing the mass conservation constraint:

$$\sum_{s=1}^{n_s} \mathbf{d}_s^D = 0 \quad \longrightarrow \quad \mathbf{d}_{n_s}^D = -\sum_{s=1}^{n_s-1} \mathbf{d}_s^D = -\mathbf{d}_s^D - \sum_{\substack{p=1 \\ p\neq s}}^{n_s-1} \mathbf{d}_p^D$$

we can derive a set of $n_s - 1$ equations defined as follows:

$$c_t \mathbf{d}_s^D = -\mathbf{B}_{ss}\mathbf{j}_s^D - \mathbf{B}_{sp}\mathbf{j}_p^D$$

where $\mathbf{B}_{ss}$ and $\mathbf{B}_{sp}$ are the diagonal and off-diagonal entries of the square matrix $[\mathbf{B}]$ of size $(n_s - 1)$ and are defined by the following equations:

$$\mathbf{B}_{ss} = \left(\frac{X_s}{\mathscr{D}_{sn_s}} + \sum_{\substack{p=1 \\ p\neq s}}^{n_s} \frac{X_p}{\mathscr{D}_{sp}} \right) \qquad \mathbf{B}_{sp} = -X_s \sum_{\substack{p=1 \\ p\neq s}}^{n_s-1} \left(\frac{1}{\mathscr{D}_{sp}} - \frac{1}{\mathscr{D}_{sn_s}} \right)$$

Thus, we have an (n_s-1) dimensional matrix of the form $c_t\, \mathbf{d}^D = -[\mathbf{B}]\, \mathbf{j}^D$ that we have implemented in US3D to solve the reduced Stefan-Maxwell equation system.

C.2 Jacobian Formulation for the Full Diffusion Model Derived from CET

The Jacobian matrix A originates from the linearization of the governing equations, and it can be written as a function of the primitive variables vector $V = [\rho_s, \mathbf{v}, T]^T$:

$$\nabla_x F = \frac{\partial F}{\partial U}\nabla_x U = A\nabla_x U = \frac{\partial F}{\partial V}\frac{\partial V}{\partial U}\nabla_x U = \underbrace{M_x N \nabla_x U}_{\text{physical space}} \equiv \underbrace{M_{eta} N \nabla_{eta} U}_{\text{computational space}}$$

Thus, introducing the Soret term in the diffusion driving force implies the addition of a block in the Jacobian matrix as a consequence of the linearization of the thermal diffusion term. The main algebraic passages are shown hereafter.

$$\text{Soret term} = \rho_s \mathbf{v}_s^{D,T} \simeq -\rho \mathcal{D}_s^T \nabla (\ln T) \simeq -\rho \mathcal{D}_s^T \frac{\nabla T}{T}$$

$$\Downarrow \text{differentiating}$$

$$\delta \left(\rho_s \mathbf{v}_s^{D,T} \right) \simeq -\frac{\rho \mathcal{D}_s^T}{T} \nabla_x (\delta T) \simeq -M_\eta(T) N(T) \frac{\partial}{\partial \eta} (\delta U)$$

where

$$M_\eta(T) = \frac{s^2}{V} \begin{pmatrix} \rho\mathcal{D}_1^T/T & \dots & 0 \\ \vdots & \rho\mathcal{D}_s^T/T & \vdots \\ 0 & \dots & \rho\mathcal{D}_S^T/T \end{pmatrix}$$

and

$$N = \frac{\partial V}{\partial U} \Rightarrow N(T) = \frac{\partial T}{\partial U} = \begin{pmatrix} \vdots & \vdots & \vdots \\ \left.\frac{\partial T}{\partial \rho_s}\right|_{s=1,S} & \frac{\partial T}{\partial (\rho \mathbf{v})} & \frac{\partial T}{\partial E} \end{pmatrix}$$